UNIVERSIDAD NACIONAL AUTÓNOMA DE MÉXICO
PROGRAMA DE MAESTRÍA Y DOCTORADO EN INGENIERÍA
ENERGÍA - FUENTES RENOVABLES

Modelación numérica de la aerodinámica del rotor de un aerogenerador de eje horizontal

TESIS
QUE PARA OPTAR POR EL GRADO DE:
Maestro en Ingeniería

PRESENTA:
Alan Saih Hernández Acosta

TUTOR PRINCIPAL
Dr. Carlos Alberto López Villalobos
Instituto de Ciencias de la Atmósfera y Cambio Climático

COTUTOR
Dr. Sergio Cuevas Garcia
Instituto de Energías Renovables

TEMIXCO, MORELOS, JUNIO 2022

UNAM
Universidad Nacional
Autónoma de México

Biblioteca Central
Dirección General de Bibliotecas de la UNAM

UNAM – Dirección General de Bibliotecas
Tesis Digitales
Restricciones de uso

DERECHOS RESERVADOS ©
PROHIBIDA SU REPRODUCCIÓN TOTAL O PARCIAL

Todo el material contenido en esta tesis esta protegido por la Ley Federal del Derecho de Autor (LFDA) de los Estados Unidos Mexicanos (México).

El uso de imágenes, fragmentos de videos, y demás material que sea objeto de protección de los derechos de autor, será exclusivamente para fines educativos e informativos y deberá citar la fuente donde la obtuvo mencionando el autor o autores. Cualquier uso distinto como el lucro, reproducción, edición o modificación, será perseguido y sancionado por el respectivo titular de los Derechos de Autor.

JURADO ASIGNADO:

Presidente:	Dr. Eduardo Ramos Mora
Secretario:	Dr. Saúl Piedra González
1er. Vocal	Dr. Sergio Cuevas García
2do. Vocal	Dr. Antonio Jarquin Laguna
3er. Vocal	Dr. Carlos Alberto López Villalobos

La tesis se realizó en el Instituto de Energías Renovables de la Universidad Nacional Autónoma de México.

TUTOR DE TESIS:

Dr. Carlos Alberto López Villalobos
Instituto de Ciencias de la Atmósfera y Cambio Climático

A mi mamá y papá.
A mi hermano.
A mis amigas y amigos.

Declaración de autenticidad

Por la presente declaro que, salvo cuando se haga referencia específica al trabajo de otras personas, el contenido de esta tesis es original y no se ha presentado total o parcialmente para su consideración para cualquier otro título o grado en esta o cualquier otra Universidad. Esta tesis es resultado de mi propio trabajo y no incluye nada que sea el resultado de algún trabajo realizado en colaboración, salvo que se indique específicamente en el texto.

Alan Saih Hernández Acosta. Temixco, Morelos, Junio 2022

Resumen

Conocer la aerodinámica del rotor de una turbina eólica es esencial para el correcto diseño geométrico de sus aspas y maximizar la potencia generada. Además, el principal problema en la optimización del diseño de un parque eólico es la dinámica de las estelas. Un aerogenerador que opera en la estela de otro tiene una disminución en la producción de energía y mayores cargas dinámicas. La teoría de momento unidimensional y la teoría BEM (Blade Element Momentum) son frecuentemente utilizadas para predecir las cargas sobre un rotor y su potencia generada. Sin embargo, ambas teorías ignoran la interacción radial que existe entre los elementos del aspa. Además, no tiene la capacidad de visualizar el campo de flujo que ocurre alrededor del rotor. Para resolver estas desventajas, aquí se implementa un modelo de dinámica de fluidos computacional (CFD, por sus siglas en inglés) que utiliza las ecuaciones de Navier-Stokes en una aproximación inviscida, el modelo de disco actuador, la teoría de elemento del aspa y el método de fronteras inmersas con el fin de predecir las cargas aerodinámicas sobre un rotor y su potencia aerodinámica.

Los resultados numéricos se contrastan contra los datos experimentales de la turbina NREL baseline. Comparando la diferencia entre los datos experimentales de la potencia y empuje con los resultados de cada método, se tiene que el error relativo mínimo de la potencia es de 1.41% para el modelo CFD y 3.93% para el método BEM. De igual forma, el error mínimo del empuje es de 0.40% y 4.96% para el modelo CFD y el método BEM, respectivamente. Por lo tanto, el modelo utilizado logra predecir con mayor precisión el empuje y potencia generada. A partir de los resultados de CFD, se encuentra que el comportamiento de las cargas en el rotor dependen de la velocidad de entrada del flujo. En general, la carga en ambas direcciones se incrementa si la velocidad de entrada también lo hace. La carga axial aumenta a partir de donde se encuentra la superficie de sustentación en el disco. Por otro lado, para la mayoría de pruebas, la carga tangencial se mantiene constante sobre todo el disco. Además, para todos los casos, la carga disminuye en el borde del disco debido a la corrección de punta que se implementa. En general, la potencia y empuje pueden ser predichos por el modelo CFD. Sin embargo, a velocidades de entrada altas, los resultados divergen de los valores experimentales. Esto puede deberse a que en este modelo simplificado ningún término de turbulencia es incorporado y, a estas velocidades, el flujo turbulento podría tener un mayor impacto en el coeficiente de potencia.

Asimismo, el modelo propuesto es capaz de predecir las características esenciales del flujo alrededor del rotor, como los vórtices de punta, el gradiente de velocidad por delante y detrás del rotor, así como la expansión de la estela. Por último, se muestra cómo la corrección de hub afecta el campo de flujo predicho por el modelo CFD y se encuentra que esta corrección no describe correctamente la incorporación de un cuerpo sólido en el flujo.

Abstract

Understanding the aerodynamics of a wind turbine's rotor is essential to properly design the blade geometry and maximize the power generation. In addition, the main problem in a wind farm layout optimization is the dynamics of the wakes. A wind turbine operating in the wake of another wind turbine has a power production reduction and a higher unsteady loading. The one-dimensional momentum theory and the BEM (Blade Element Momentum) theory are frequently used to predict the loads on a rotor and its power generation. However, both theories neglect the radial interaction between the blade elements. Moreover, another drawback is not being able to visualize the flow field that occurs around the rotor.

Therefore, a computational fluid dynamics (CFD) model is implemented using the approximately inviscid Navier-Stokes equations, the actuator disc model, the blade element theory, and the immersed boundary method to predict the loads on a rotor and its power output. The numerical results are compared against the experimental data of the NREL baseline turbine. The widely used BEM method and the CFD model results were compared. Taking the difference of the results of the power of each method against the experimental data, the minimum error for the CFD model is 1.41% and for the BEM method is 3.93%. Likewise, for thrust, the minimum errors are 0.40% y 4.96% using the CFD model and BEM method, respectively. Therefore, the CFD model can predict more accurately the power and thrust. The CFD results show that the behavior of the loads on the rotor depends on the inflow velocity. When the speed increases, the load does too. The axial load grows from where the lifting surface begins. Besides, the tangential load remains constant for most tests throughout the disc. Also, the load decreases at the edge of the disc for all cases due to the implemented tip correction.

The power and thrust can be predicted by the CFD model. However, the results diverge from the experimental values at high incoming speeds. This may be because no turbulence term is incorporated in this model, and at these speeds, the turbulent flow could have a greater impact on the power. Likewise, the proposed model can predict some flow characteristics around the rotor, such as the tip vortices, the velocity gradient around the rotor, and the expansion of the wake. Finally, it is shown how the hub correction affects the flow field predicted by the CFD model, and it is found that this correction does not properly describe the incorporation of a solid body in the flow.

Contents

List of Figures **xi**

List of Tables **xiii**

1 Introduction **1**
- 1.1 Brief history of wind energy 1
- 1.2 Problem statement 3
- 1.3 Background 3
- 1.4 Objectives 5
  - 1.4.1 Specific objectives 5
- 1.5 Scope of work 5

2 Mathematical formulation **7**
- 2.1 Actuator disc 7
  - 2.1.1 One-dimensional axial momentum theory 7
- 2.2 Body forces 9
- 2.3 Blade element/momentum theory 12
  - 2.3.1 Tip correction 15
  - 2.3.2 Hub correction 15
- 2.4 Model formulation 17

3 Numerical Implementation **19**
- 3.1 Numerical solution of the momentum equations 19
- 3.2 Immersed boundary 24
  - 3.2.1 Structure of the front 24
  - 3.2.2 Interpolating the front properties onto the fixed grid 25
- 3.3 Numerical procedure 26

4 Results **29**
- 4.1 Airfoil data 29
- 4.2 The constant loaded rotor disc 31

4.2.1 Numerical tests 31
4.2.2 Numerical results 34
4.3 Simulation on NREL baseline wind turbine 38
4.3.1 Flow field properties 46
4.3.2 Hub correction assessment 51

5 Conclusions 55

A Supplementary data 57
A.1 Airfoil data 57
A.2 Blade geometry 61

Bibliography 63

List of Figures

1.1 Persas windmills [2]. 2
1.2 James Blyth's turbine [3]. 2

2.1 Control volume given by the stream tube encompassing the actuator disc for one-dimensional. Adapted from Sorensen [19]. 8
2.2 Cross-section of a blade element located at radius r. Adapted from Behrouzifar and Darbandi [13]. 10
2.3 Different corrections for overloaded rotors against empirical data [30]. . . 17
2.4 Actual domain (a) and computational domain (b). 18

3.1 Regular grid. 20
3.2 Velocities locations and pressure corrections on the staggered grid. . . . 23
3.3 Front sketch [33]. 25
3.4 Area of weighting to interpolate properties from the fixed grid to the front. 26
3.5 Flowchart describing the numerical steps to solve the model used. 27

4.1 S809 airfoil coordinates. 30
4.2 Lift (a) and drag (b) coefficients for S809 airfoil. 30
4.3 Averaged axial factor for different radial lengths 32
4.4 Averaged axial factor for different axial lengths 33
4.5 Averaged axial factor through the dimensionless time for $C_T = 0.8$. . . . 34
4.6 Dimensionless axial force for $C_T = 0.4$. 35
4.7 Axial velocity (a) and axial factor (b) along the radius for several thrust coefficients. 35
4.8 Pressure along the axial direction for r/R=0.5. 36
4.9 Axial (a) and radial (b) velocity upstream and downstream for $C_T = 0.4$ at $r/R = 0.5$. 37
4.10 Velocity field for $C_T = 0.4$. The disc is represented by a straight line. . . 38
4.11 Tip vorticity (a) and streamlines (b) for a constant loaded rotor disc with $C_T = 0.4$. The disc is represented by a straight line. 38
4.12 Axial velocity for several inflow values. 39

4.13 Radial velocity for several inflow values. 39
4.14 Tangential velocity for several inflow values. 40
4.15 Axial (a) and tangential (a) factor along the rotor. 41
4.16 Corrections product. 41
4.17 Axial (a) and tangential (b) forces along the rotor. 42
4.18 Thrust (a) and torque (b) calculated by BEM and CFD at different inflow velocities. 43
4.19 Power (a) and thrust (b) calculated by CFD and BEM theory, compared with experimental data. 44
4.20 Reynolds number (a) and attack angle (b) calculated by BEM and CFD at different inflow velocities. 45
4.21 Axial (a) and tangential (b) dimensionless forces imposed for the baseline turbine for $U_\infty = 10\ m/s$. 46
4.22 Velocity field for $U_\infty = 10\ m/s$. The disc is represented by a straight line. 47
4.23 Streamlines for $U_\infty = 10\ m/s$. The disc is represented by a straight line. 48
4.24 Vorticty field for $U_\infty = 10\ m/s$. The disc is represented by a straight line. 48
4.25 Distributions of axial (a), radial (b) and tangential (c) velocities at various downstream locations for three inflow values (red: $U_\infty = 5\ m/s$, green: $U_\infty = 10\ m/s$, blue: $U_\infty = 15\ m/s$). 50
4.26 Axial (a) and tangential (b) force in the radial direction. (B-HC: Both force directions corrected; T-HC: Just tangential direction corrected; W-HC: Both force directions without correction). 52
4.27 Axial (a) and tangential (b) velocity in the radial direction. (B-HC: Both force directions corrected; T-HC: Just tangential direction corrected; W-HC: Both force directions without correction). 52
4.28 Axial velocity applying hub correction in both directions (a), just tangential direction (b) and without correction (c). The flow field is mirrored to appreciate the hub interaction. The disc is represented by a straight line. 54

List of Tables

4.1 Averaged axial factor and relative error, ϵ, for several L_r. 32
4.2 Averaged axial factor and relative error, ϵ, for several L_x. 33

A.1 S809 airfoil data. 57
A.2 Blade geometry of NREL Baseline. 61

Chapter 1

Introduction

This study deals with a numerical implementation of incompressible Navier-Stokes equations and the axisymmetric actuator disc model to describe the aerodynamics of horizontal axis wind turbine rotors. A permeable disc represents the wind turbine rotor and allows the flow to pass through it while the disc disturbs the flow. The finite volume method is used to discretize the equations in the spatial and temporal dimensions. The immersed boundary method is implemented to represent the rotor inside the domain and to spread the force onto the fixed grid where the properties are computed.

1.1 Brief history of wind energy

A wind turbine is a device that converts the kinetic energy of the wind into electricity. For a long time, the wind has been used as a power source, such as in sailing boats that travelled long or mills to grind grains or pump water. The Herón of Alenxandría machine was one of the first ones recorded [1], which consisted of a windmill that provided air to a pipe organ. Most windmills appeared in Europe, and they incorporated a horizontal axis, although some vertical axis windmills could be seen as made by the ancient Persians (see Figure 1.1).

In Scotland, James Blyth marked the beginning of the modern wind turbines by building a wind turbine from sailcloth. The output power of the turbine was dedicated to charging batteries whose energy was used in his house. Figure 1.2 shows the James Blyth turbine. We can appreciate the size difference between the person and the wind turbine.

In 1888, in Cleveland, Ohio, Charlie Brush built a wind turbine with a radius of 17 meters and 144 blades, generating 12 kW. At the same time, in Denmark, Poul La Cour made experiments on airfoils for wind turbines and proved that wind turbines with fewer blades are more efficient in producing electricity. Marcellus Jacob designed smaller wind turbines. These devices were similar to the current turbines, with a hor-

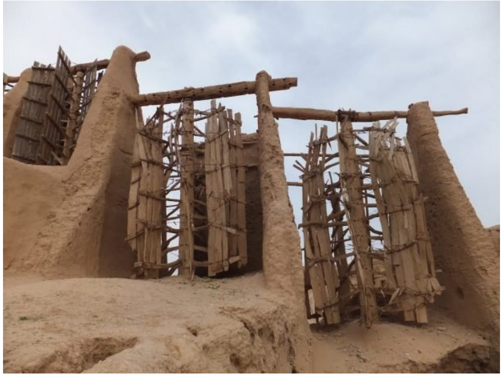

Figure 1.1: Persas windmills [2].

izontal axis and three blades. During the Second World War, the interest in wind energy raised again. This new resurgence led to the building of F.L. Smith wind turbines, which used the stall regulation (reduction of lift by modifying the attack angle) and upwind direction (namely, the front of the wind turbine is set opposite to the wind direction).

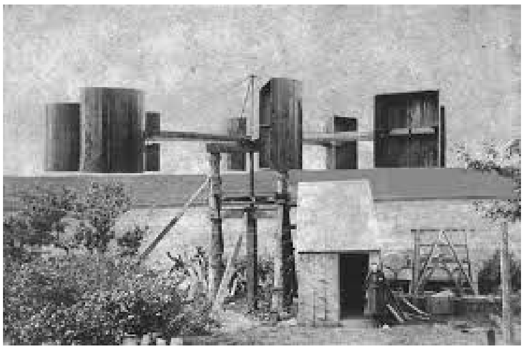

Figure 1.2: James Blyth's turbine [3].

As of the date of this writing, for onshore applications, the large-scale wind turbines can produce around 2 MW of power, and their rotor diameters are a little less than 100 meters. However, the tendency is to develop bigger turbines with larger rotors. The Haliade-X is the biggest wind turbine installed for tests, and it can produce 12 MW with a rotor diameter of 220 meters.

1.2 Problem statement

The rotor aerodynamics of a wind turbine is a complex problem. Many factors can affect the performance of a rotor. The turbulence intensity can increment the available power on the site but, at the same time, affect the wind turbine structure [4]. Also, the wind resource depends on the geographic location and local terrain; even the wind turbines reside inside the atmospheric boundary layer (e.g., <300 m) [4]. In wind farms, wake interaction between wind turbines impacts power production. The micro-scale processes in which a wind turbine plant is involved are below one kilometer and, generally, have grid spacing between 5 and 100 meters horizontally. This large space to explore leads to use grids with a huge number of cells, in the order of millions [5], requiring expensive computational efforts.

The BEM theory is a well-known tool for describing wind turbine loads and power production. This theory is simple to apply and can describe the rotor behavior. However, it does not provide information about the flow around the turbine. Also, the BEM theory neglects the radial interaction blade to blade, which influences the performance of each element, while CFD computations allow knowing the flow field that encompasses the rotor and the radial interaction to be taken into account.

In this work, for the sake of simplification, an inviscid model is used to reproduce the wind turbine performance and flow field, focusing on the general characteristics. The forces are computed using the blade element theory and specific airfoil data for the turbine. Also, the aeroelastic effects are not considered. The implementation of the forces given by the rotor to the fixed grid are carried out employing the immersed boundary method, which makes a smooth distribution of the force to the surroundings avoiding numerical oscillations when implementing punctual forces.

The benefit of modeling the rotor aerodynamics is that aerodynamic properties can be calculated with better precision since the radial interference between the blade is taken into account. Also, it is possible to know the flow around the turbine, which is important to know to asses the influence on the performance of the turbines behind, as in a wind farm. Moreover, due to the simplification of the model, the fine mesh to capture small-scale turbulent effects is unnecessary. Therefore, a coarser grid can be used, reducing the computational time.

1.3 Background

The aerodynamics of a wind turbine has been studied for a long time. However, there are unknowns to be resolved as the understanding of the physics of atmospheric flow, material and system dynamics of individual wind turbines, optimization and control of wind plants, wind energy resource quantification, wind array turbines optimization, and turbulent wakes, among others [6][4]. This work aims to enhance the wind turbine arrays in wind farms. In an actual wind farm, the interaction between the flow and structure becomes relevant since the disturbance of the wind can impact the performance of the wind turbines around. As a first step to improving the wind turbine array, it is fundamental to understand the behavior of an isolated wind turbine and effectively predict its performance and interaction with the flow. After this, several add-ons can be incorporated into the new models, such as the shear boundary layer, atmospheric turbulence, and interaction turbine-turbine.

The methodology to know the aerodynamic load proposed by Betz [7] indicates the maximum power that can be obtained from the wind is 59.3%. However, this method is based on the one-dimensional theory and neglects the rotor's rotation and the power losses. Other analytical methods are developed by Glauert [8], Joukowsky [9] and Burton [10] where the rotational effects and the difference in pressure occurring in front and behind the rotor are included in the analysis.

Glauert proposed the Blade Element Momentum(BEM) theory to compute the main properties of the rotor of a wind turbine. It was based on the one-dimensional momentum theory, which uses the momentum equations in just one direction, and the blade element theory, which splits the blade into elements, and the properties are computed for each of them. The BEM theory is widely used, and several corrections have been used to achieve better results, such as the tip or hub correction or even employing a dynamic wake.

The increment in computing power has led to a new Computational Fluid Dynamics(CFD) approach to solve the problem. The new models describe the flow around the rotor, the wake, and the interaction with other rotors behind. In the works made by Sorensen and Kock [11], and Mikkelsen [12], the Vorticity-Stream functions are used to solve the flow field. Also, the actuator disc concept is implemented to add a constant load along with the rotor and apply it to the flow field. Several works have been made to predict the wake behind the rotor [13][14][15] since this has a major influence on the aerodynamic performance of a wind farm. Some corrections can be used to get a more realistic result. Shen et al. [16] used a tip correction combined with the Navier-Stokes equations to solve the aerodynamic properties of a rotor. Another technique applied to the problem is the actuator line, in which the load is distributed along a line representing the blade forces, as exposed by Sorensen and Shen [14] to describe the performance and the wake of the rotor. Martínez et al. [17] presented a comparison between the actuator disc and actuator line. The immersed boundary method results is a way to apply the blade forces on the domain since it has the advantage of interpolating the properties from the fixed grid where the Navier-Stokes equations are computed and the front that describes the object, namely, the rotor. According to Yang and Sotiropoulos

[18], the nacelle can be modeled by a front made by points that describe it. Also, a smooth function is used to interpolate the velocities and to spread the force applied by the rotor.

1.4 Objectives

The main objective is

> *To develop a numerical fluid dynamic code based on an actuator disc concept to simulate the aerodynamic properties of a horizontal axis wind turbine.*

1.4.1 Specific objectives

The specific objectives are

- To implement the finite volume and immersed boundary methods to determine the velocity and force field.
- To determine the power production.
- To determine the axial and tangential momentum acting on the rotor.
- To validate the results from the numerical code by comparing them against experimental data.

1.5 Scope of work

Due to the difficulties of simulating a complete wind turbine and the atmospheric conditions that affect it, this work aims to generate a simple computational model to predict the power generation, loads, and flow field around the rotor of an isolated wind turbine. In the proposed model, an actuator disc represents the rotor. The forces are computed from the actual geometry of the blades, which are imposed on the computational domain using the immersed boundary method. The scope of the work is limited to the rotor, without including the nacelle or the tower. Moreover, the atmospheric boundary layer and the turbulent effects are not considered. Since the rotor is included as a force that perturbs the flow, the boundary layer between fluid and structure is not solved.

Chapter 2

Mathematical formulation

2.1 Actuator disc

The Actuator Disc concept is an idealized representation of a rotor, consisting of a permeable disc that allows the flow to pass while imposing force. In this concept, there is a pressure difference on the rotor plane without a discontinuity on the axial velocity [19]. Froude [20] introduced the actuator disc concept based on the work of Rankine [21] on the momentum theory of propellers. One of the fundamental results was presented for the actuator disc plane velocity, which equals one half of the upstream and far wake wind speed sum. The analysis by Betz [7] showed that the maximum extraction of energy possible from a wind turbine rotor is 59.3 % of the incoming kinetic energy.

A major step forward in modeling flow through rotors came with developing the generalized momentum theory and the introduction of the Blade Element Momentum (BEM) method by Glauert [8]. The BEM theory is computationally inexpensive because each blade element is considered a two-dimensional airfoil [22]. Moreover, additional corrections have to be made, such as tip and hub losses, heavily loaded rotors, yaw correction, or dynamic wake can be done to model the more complex unsteady aerodynamic phenomena [19], keeping the low computational time. In industry, it is widely used to design a simpler optimum blade. This first approach can be used as the beginning of a general blade design analysis [23].

2.1.1 One-dimensional axial momentum theory

The one-dimensional axial momentum theory [19] assumes an incompressible uniform flow with a constant velocity passing an actuator disc. The flow velocity is the same on the whole disc, which means that axial symmetry exists. The flow can not cross the control volume given by the stream tube encompassing the actuator disc (see Figure 2.1). Also, the flow is treated as inviscid, so no loss inside the control volume is happening. Consider an axial flow with speed U_∞, which moves through an actuator

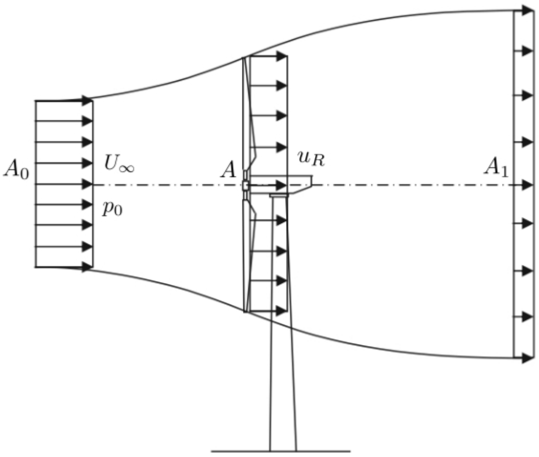

Figure 2.1: Control volume given by the stream tube encompassing the actuator disc for one-dimensional. Adapted from Sorensen [19].

disc of area A and constant axial load T, where u_R is the velocity on the rotor plane and u_1 the velocity on the ultimate wake. Remember that the pressure at the entrance is the same as on the ultimate wake without disturbance, namely, $p_1 = p_0$, and ρ is the air density. In Figure 2.1, A_0 and A_1 are the areas upstream and downstream, respectively.

From mass conservation, the mass flow ratio, $\dot{m}$, must be constant on each section of the stream tube. Thus,

$$\dot{m} = \int \rho u dA = \rho U_\infty A_0 = \rho u_R A = \rho u_1 A_1. \tag{2.1}$$

Axial momentum balance results on the next equation for the stream tube shown in Figure 2.1.

$$T = \dot{m}(U_\infty - u_1) = \rho u_R A(U_\infty - u_1). \tag{2.2}$$

Assuming the pressure in the wake is equal to the pressure upstream, $p_1 = p_0$, and that the lateral pressure acting on the stream tube is zero, and then applying the Bernoulli equation in front and behind the rotor, we obtain

$$\Delta p = \frac{1}{2}\rho(U_\infty^2 - u_1^2), \tag{2.3}$$

where the pressure difference represents the thrust $T = A\Delta p$. Combining equations 2.2 and 2.3, we get

$$u_R = \frac{1}{2}(U_\infty + u_1). \tag{2.4}$$

Introducing the axial interference factor

$$a_a = \frac{U_\infty - u_R}{U_\infty}, \tag{2.5}$$

we get

$$u_R = (1 - a_a)U_\infty. \tag{2.6}$$

Combining equations 2.4 and 2.6

$$u_1 = (1 - 2a_a)U_\infty. \tag{2.7}$$

Inserting equations 2.6 and 2.7 in Eq. 2.2, we can obtain

$$T = 2\rho A U_\infty^2 a_a (1 - a_a) \tag{2.8}$$

and

$$P = u_R T = 2\rho A U_\infty^3 a_a (1 - a_a)^2. \tag{2.9}$$

Introducing the dimensionless coefficients for thrust and power, respectively

$$C_T = \frac{T}{\frac{1}{2}\rho A U_\infty^2}, \qquad C_P = \frac{P}{\frac{1}{2}\rho A U_\infty^3}, \tag{2.10}$$

we get

$$C_T = 4a_a(1 - a_a), \qquad C_P = 4a_a(1 - a_a)^2. \tag{2.11}$$

Obtaining the derivative of the power coefficient with respect to the axial interference factor, we can get the maximum obtainable power as

$$C_{P,max} = \frac{16}{27} = 0.593, \qquad \text{with} \qquad a_a = \frac{1}{3}. \tag{2.12}$$

This result is known as the Betz limit and declares the maximum power extracted, namely, the 59.3%. This result does not include the losses because of the wake rotation. Therefore, it means a conservative upper maximum. It should be noted that the One-dimensional theory is only valid for values of a_a between 0 and 0.5. For higher values, results of u_1 are negative (see Eq. 2.7).

2.2 Body forces

We recall the Navier-Stokes momentum equation

$$\rho\left(\frac{\partial \mathbf{u}}{\partial t} + (\mathbf{u} \cdot \nabla)\mathbf{u}\right) = -\nabla p + \mu \nabla^2 \mathbf{u} + \mathbf{f_b}, \tag{2.13}$$

where the first term on the left-hand side is the change in velocity over time, and the second one is the convective term. The first term on the right-hand side is the pressure gradient, and the second one is the viscous term. The last term, $\mathbf{f_b}$, represents the body forces acting on the rotor and they are obtained by an approach to the blade element theory and two-dimensional tabulated airfoil data. Figure 2.2 shows a blade element on the plane (x, θ), fixed at a distance r on the blade.

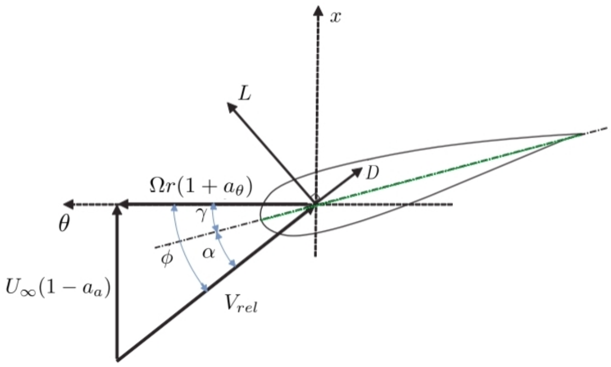

Figure 2.2: Cross-section of a blade element located at radius r. Adapted from Behrouzifar and Darbandi [13].

The process of computing the force that takes place on the rotor is similar as presented by Behrouzifar and Darbandi [13]. The axial and tangential factors are

$$a_a = 1 - \frac{u_R}{U_\infty}, \qquad a_\theta = \frac{w_R}{r\Omega}, \tag{2.14}$$

where u_R and w_R are the axial and tangential velocities on the rotor plane, respectively. U_∞ being the incoming velocity far away and $r\Omega$ the tangential velocity of the chosen blade section. The tangential and axial components are described in the inertial reference frame by

$$v_\theta = (1 + a_\theta)r\Omega = w_R + r\Omega, \qquad v_x = (1 - a_a)U_\infty. \tag{2.15}$$

Thus, the local velocity relative to the rotating blade is

$$V_{rel} = (v_\theta, v_x). \tag{2.16}$$

As it is shown in Figure 2.2, the angle between the rotor plane and V_{rel}, flow angle, can be computed from the equation

$$\phi = \tan^{-1}(v_x/v_\theta), \tag{2.17}$$

which is called flow angle. Therefore, the angle of attack is obtained following the relation

$$\alpha = \phi - \gamma - \theta_p, \tag{2.18}$$

where γ is the twist angle, which is the angle of deformation of each section along the blade. On the other hand, θ_p is the pitch angle of the wind turbine, this angle is at which the entire blade moves and it is set by the wind turbine control system. After knowing the relative velocity V_{rel}, we can compute the blade force per unit span-wise length as

$$\frac{d\mathbf{F}}{dr} = \frac{1}{2}\rho V_{rel}^2 c(C_L\hat{e}_L + C_D\hat{e}_D), \tag{2.19}$$

where c refers to the airfoil chord, namely, the straight line joining the edges of the airfoil (see dashed green line in Figure 2.2). C_L and C_D are the lift and drag coefficients obtained using two-dimensional airfoil data. Moreover, $\hat{e}_L$ and $\hat{e}_D$ are the unit vectors in the lift and drag directions, respectively. Also, dr is a differential length along the r-direction.

In order to simplify the blade geometry inside the computational domain, we can assume a blade with a constant thickness dx. Thus, each element has the same differential volume $dV = 2\pi r dr dx$. Combining this with the Eq. 2.19, the force per volume for a total number of B blades can be calculated using the following equation

$$\mathbf{f_b} = B\frac{d\mathbf{F}}{dV} = \frac{1}{4\pi r dx}B\rho V_{rel}^2 c(C_L\hat{e}_L + C_D\hat{e}_D). \tag{2.20}$$

The aerodynamic loads should be implemented as source and sink terms in the corresponding equations that will be shown later. Therefore, the force is decomposed in different directions for the cylindrical coordinates. Thus, the distribution of the force per volume for the axial, radial and tangential components can be computed by the following equations, respectively

$$f_x = \frac{1}{4\pi r dx}B\rho V_{rel}^2 c(C_L\cos\phi + C_D\sin\phi), \tag{2.21}$$

$$f_r = 0, \tag{2.22}$$

$$f_\theta = \frac{1}{4\pi r dx}B\rho V_{rel}^2 c(C_L\sin\phi - C_D\cos\phi). \tag{2.23}$$

Since we are dealing with a two-dimensional airfoil in the $x - \theta$ plane, the resultant forces are only projected in these two directions. In the simplified model presented in this work, the three-dimensional effects occurring on the airfoils with a large spanwise are neglected. The thrust and power can be calculated by integrating the lift and drag forces in the radial direction, which yields the following equations

$$\text{Thrust} = T = \frac{1}{2}\rho B \sum_{k=1}^{k=N} V_{rel_k}^2 c_k (C_{Lk}\text{cos}\phi_k + C_{Dk}\text{sin}\phi_k) dr_k, \tag{2.24}$$

$$\text{Power} = P = \frac{1}{2}\rho B\Omega \sum_{k=1}^{k=N} r_k V_{rel_k}^2 c_k (C_{Lk}\text{cos}\phi_k + C_{Dk}\text{sin}\phi_k) dr_k, \tag{2.25}$$

where k is the indexing variable of the section and N is the total number of sections that compose the blade.

2.3 Blade element/momentum theory

Glauert developed the Blade Element Momentum (BEM) theory to describe the aerodynamics of the rotor of a propeller and wind turbine. Moreover, the BEM theory is also implemented to design and optimize wind turbine rotor blades. The BEM theory combines two theories, the first one is the blade-element theory, and the second one is the one-dimensional momentum theory. It is possible to obtain a closed system of equations to compute the induced velocities and the loads acting on the rotor if both methods are combined.

We use the general derivation of the equation exposed in literature with some corrections for loaded rotors [19][24][23]. The axial load and torque defined from the blade-element theory are as follows

$$\frac{dT}{dr} = BF_x = \frac{1}{2}\rho c B V_{rel}^2 C_a, \tag{2.26}$$

$$\frac{dQ}{dr} = BrF_\theta = \frac{1}{2}\rho c B r V_{rel}^2 C_t, \tag{2.27}$$

where c is the chord, B is the total number of blades, and V_{rel} is the relative velocity of the flow with respect to the azimuthal direction, as it can be seen in Figure 2.2. The loads are represented by F_x and F_θ in the axial and tangential directions, respectively. C_a and C_t correspond to the two-dimensional force coefficients, defined as

$$C_a = \frac{F_x}{1/2\rho c V_{rel}^2}, \tag{2.28}$$

$$C_t = \frac{F_\theta}{1/2\rho c V_{rel}^2}. \tag{2.29}$$

Projecting the lift and drag coefficients, we can build the force coefficients as

$$C_a = C_L\text{cos}\phi + C_D\text{sin}\phi, \tag{2.30}$$

$$C_t = C_L \text{sin}\phi - C_D \text{cos}\phi, \tag{2.31}$$

where ϕ is the flow angle, the angle formed between the relative velocity and the rotor plane, C_L and C_D are the lift and drag coefficients, which are obtained using two-dimensional airfoil data tabulated that depend on the angle of attack and Reynolds number. The angle of attack α is given as follows

$$\alpha = \phi - \gamma - \theta_p, \tag{2.32}$$

being γ the twist angle and θ_p the pitch angle. Remembering axial and tangential coefficients given in Eq. 2.14 and using Figure 2.2, we can deduce that

$$\text{sin}\phi = \frac{U_\infty(1-a_a)}{V_{rel}}, \qquad \text{cos}\phi = \frac{\Omega r(1+a_\theta)}{V_{rel}}. \tag{2.33}$$

From these two relations, we get

$$V_{rel}^2 = \frac{U_\infty^2(1-a_a)^2}{\text{sin}^2\phi} = \frac{U_\infty(1-a)\Omega r(1+a_\theta)}{\text{sin}\phi\text{cos}\phi}. \tag{2.34}$$

Combining these relations with Eqs. 2.26 and 2.27, we can get

$$\frac{dT}{dr} = \frac{\rho B c U_\infty^2(1-a_a)^2}{2\text{sin}^2\phi} \cdot C_a, \tag{2.35}$$

$$\frac{dQ}{dr} = \frac{\rho B c U_\infty(1-a_a)\Omega r^2(1+a_\theta)}{2\text{sin}\phi\text{cos}\phi} \cdot C_t. \tag{2.36}$$

Now, from the axial momentum theory, we can compute the axial load as

$$\frac{dT}{dr} = \rho(U_\infty - u_1)2\pi r u_R = 4\pi\rho r U_\infty^2 a_a(1-a_a), \tag{2.37}$$

where u_R is the axial velocity in the rotor plane given as

$$u_R = U_\infty(1-a_a), \tag{2.38}$$

and u_1 is the axial velocity in the ultimate wake calculated as

$$u_1 = U_\infty(1-2a_a). \tag{2.39}$$

As a result of the One-dimensional momentum theory, the induced velocity in the wake is twice that in the plane of the rotor. Also, it is assumed that pressure is recovered in the far wake. Thus, the pressure upstream and downstream of the rotor are equal.
After applying the momentum theory, we can obtain

$$\frac{dQ}{dr} = \rho r u_\theta 2\pi r u_R = 4\pi\rho r^3\Omega U_\infty a_\theta(1-a_a), \tag{2.40}$$

where $u_\theta = 2\Omega r a_\theta$ is the induced tangential velocity downstream of the rotor. Putting together the Eqs. 2.35 with 2.37 and the Eqs. 2.36 with 2.40, we can get

$$a_a = \frac{1}{4\sin^2\phi/(\sigma C_a)+1}, \tag{2.41}$$

$$a_\theta = \frac{1}{4\sin\phi\cos\phi/(\sigma C_t)-1}, \tag{2.42}$$

where $\sigma = Bc/2\pi r$ is the local solidity. The two last equations are the most important expressions in the BEM theory.

The total system of equations is nonlinear and implicit, thus, we need to use an iterative technique to solve it. A solution procedure to follow is

1. Divide the rotor into a sufficient number of blade elements. The current procedure will be applied for each element.
2. Assume an initial value for a_a and a_θ. It could be based on the last value obtained for the last element solved, or simply setting $a_a = 1/3$ and $a_\theta = 0$.
3. Obtain the flow angle using the expression: $\phi = \tan^{-1}\left(\frac{1-a_a}{\lambda_r(1+a_\theta)}\right)$, with $\lambda_r = \lambda(r/R)$, where $\lambda = \frac{\Omega R}{U_\infty}$ is the tip speed ratio and R is the rotor radius.
4. Calculate the angle of attack, $\alpha = \phi - \gamma - \theta_p$, and from this and the Reynolds number ($Re = \frac{U_{rel}c}{\nu}$), determine C_L and C_D from tabulated aerodynamic data of the airfoil.
5. Compute C_a and C_t.
6. Compute the new factors a_a and a_θ. Continue the procedure until convergence and move to the next element.

As seen in the solution procedure, a_a and a_θ are forced to converge to a specific value. Thus we ensure a physically representative value. After calculating the induced velocities, the thrust and power are computed by the Eqs. 2.24 and 2.25, respectively.

The axial symmetry assumption implies that the induced velocities on the blade are not dependent on the number of blades of the rotor. Therefore, the vortex shed from the ends of the rotor form a constant stream surface. However, the pressure difference in front and behind the blade should decrease on the tip because of the crossed flow effects. To consider this effect, the load is modified by a tip correction.

2.3.1 Tip correction

There are different equations to make the tip correction, some of them are discussed by Clifton-Smith [25] and Shen et al. [26]. One of the most popular equations is the one derived by Glauert from the equation for Prandtl loss, given by

$$F_{tip} = \frac{2}{\pi}\cos^{-1}\left[\exp\left(-B\frac{R-r}{2r\sin\phi}\right)\right], \tag{2.43}$$

where B is the number of blades, R the radius of the rotor, r the local radius and ϕ the flow angle.
Other equation to correct the tip loss is the one proposed and applied by Shen et al. [27][28]. Which is given by

$$F_{tip} = \frac{2}{\pi}\cos^{-1}\left[\exp\left(-g\frac{B(R-r)}{2r\sin\phi}\right)\right], \tag{2.44}$$

where the variables are similar to the equation proposed by Glauert. However, the new factor g depends on the number of blades, TSR, and chord distribution, although for simplicity, the function will only depend on the variable $B\Omega R/U_\infty$, so g is computed as

$$g = \exp(-c_1(B\Omega R/U_\infty - c_2)) + c_3, \tag{2.45}$$

here c_1, c_2 and c_3 are the correction coefficients, and their values are 0.125, 21 and 0.1, respectively.

2.3.2 Hub correction

Similar to tip loss correction, the hub correction works to correct the induced velocity resulting from a vortex shed near the rotor's hub. An equation to apply this correction is much like the Prandtl tip loss model, and it is given by

$$F_{hub} = \frac{2}{\pi}\cos^{-1}\left[\exp\left(-B\frac{r-R_{hub}}{2r\sin\phi}\right)\right]. \tag{2.46}$$

Other way to account for the influence of the hub and the effects of the non-lifting parts of the rotor is to introduce a vortex core of size δ [29], by the equation

$$F_{hub} = 1 - \exp\left[-a\left(\frac{x}{\bar{\delta}}\right)^{b}\right], \tag{2.47}$$

where $\bar{\delta} = \frac{\delta}{R}$ is the dimensionless radial distance to the point where the maximum azimuthal velocity is achieved, this point commonly corresponds to the point where the lifting surface starts on the rotor. The local radius is represented by $x = \frac{r}{R}$. The

two parameters, a and b, are introduced to fit the inner viscous core of a vortex, in this work $a = 2.335$ and $b = 4$, according to Sorensen et al. [29].
In the blade element theory, the corrections can be applied just multiplying the tip corrections by the drag and lift coefficients as

$$C_{D_{corr}} = C_D F_{tip} F_{hub}, \tag{2.48}$$

$$C_{L_{corr}} = C_L F_{tip} F_{hub}. \tag{2.49}$$

And C_D and C_L should be replaced by $C_{D_{corr}}$ and $C_{L_{corr}}$, respectively.

The Actuator disc theory involves a constant surface resulting in a circular uniform vortex shed on the wake. However, in an actual wind turbine, the vortex is shed from the tip of each blade, resulting in a different vortex system. Also, close to the tip, the circulation must decrease because of the compensation between the lower and upper side of an airfoil, which is not taken into account in the Actuator disc theory. To incorporate this effect, a tip correction is included. Also, the hub presence as a solid rigid affects the velocity on the center of the rotor; therefore, it is convenient to use a hub correction. When the tip and hub corrections are implemented, the Eqs. 2.41 and 2.42 should be modified as follows

$$a_a = \frac{1}{4F\text{sin}^2\phi/(\sigma C_a) + 1}, \tag{2.50}$$

$$a_\theta = \frac{1}{4F\text{sin}\phi\text{cos}\phi/(\sigma C_t) - 1}, \tag{2.51}$$

where F is the product of the tip and hub corrections if there were both corrections. However, when the rotor is overloaded, Eq. 2.50 gives incorrect predictions, as it is discussed by Manwell et al. [23] and Buhl [30]. Figure 2.3 depicts different corrections for overloaded rotors found in literature against empirical data. After $a > 0.4$, the results of the one-dimensional theory begin to deviate from the empirical data and it becomes necessary to incorporate a correction for this region. Therefore, we introduce an empirical expression to take into account the overload condition. When the local thrust coefficient is greater that 0.96 ($C_{Tr} > 0.96$), the Eq. 2.50 is replaced by

$$a_a = \frac{1}{F}[0.143 + \sqrt{0.0203 - 0.6427(0.889 - C_{Tr})}], \tag{2.52}$$

where $F = F_{tip}\ F_{hub}$ and

$$C_{Tr} = \frac{\sigma(1 - a_a)^2(C_L\text{cos}\phi + C_D\text{sin}\phi)}{\text{sin}^2\phi}. \tag{2.53}$$

The Eq. 2.52 replaces the equation without the overloaded rotor correction (Eq. 2.50). This new equation is solved iteratively as described above.

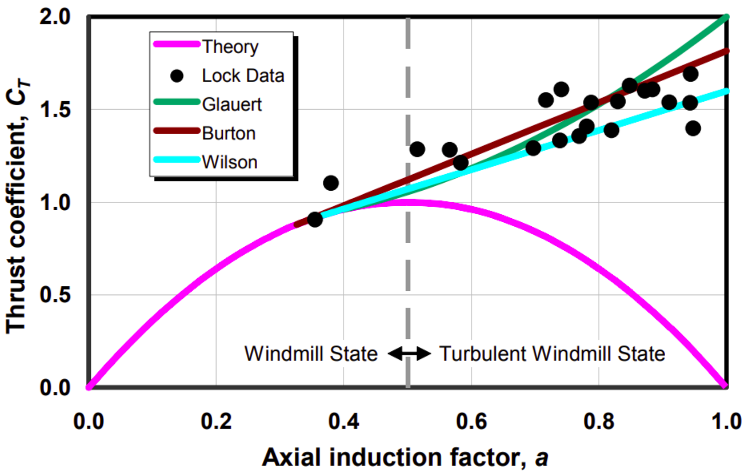

Figure 2.3: Different corrections for overloaded rotors against empirical data [30].

2.4 Model formulation

First, we obtain a new set of dimensionless variables given as

$$\mathbf{u}^* = \frac{\mathbf{u}}{U_\infty}, \qquad p^* = \frac{p}{\rho U_\infty}, \qquad \mathbf{x}^* = \frac{x}{R}, \qquad t^* = \frac{t}{R/U_\infty}. \tag{2.54}$$

We replace the new set of dimensionless variables on the Navier-Stokes equation (Eq. 2.13) and from now on, we omit the symbol * on the dimensionless variables in order to have a simpler notation. Remembering that it refers to them unless otherwise clarified. Thus, assuming incompressible, unsteady and using the cylindrical coordinates given by (x, r, θ) with the velocities (u, v, w), respectively, and using the dimensionless variables given previously, the Navier-Stokes equations are

Momentum on x

$$\frac{\partial u}{\partial t} + (\mathbf{u} \cdot \nabla)u = -\frac{\partial p}{\partial x} + \frac{1}{Re}\nabla^2 u - f_x. \tag{2.55}$$

Momentum on r

$$\frac{\partial v}{\partial t} + (\mathbf{u} \cdot \nabla)v - \frac{w^2}{r} = -\frac{\partial p}{\partial r} + \frac{1}{Re}\left(\nabla^2 v - \frac{v}{r^2}\right) + f_r. \tag{2.56}$$

Momentum on θ

$$\frac{\partial w}{\partial t} + (\mathbf{u} \cdot \nabla)w + \frac{vw}{r} = \frac{1}{Re}\left(\nabla^2 w - \frac{w}{r^2}\right) + f_\theta. \tag{2.57}$$

Mass conservation

$$\frac{\partial u}{\partial x} + \frac{1}{r}\frac{\partial vr}{\partial r} = 0. \tag{2.58}$$

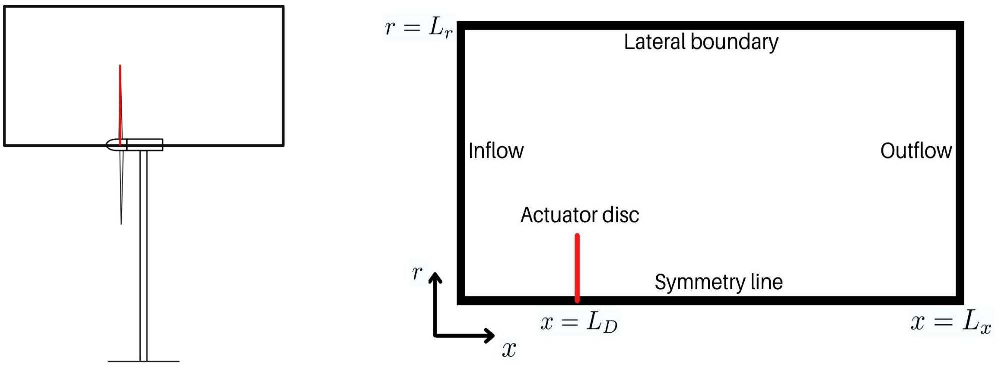

(a) Actual domain.

(b) Computational domain.

Figure 2.4: Actual domain (a) and computational domain (b).

The previous body forces, $\mathbf{f_b}$, should be multiplied by a new factor becoming in $\mathbf{f} = (f_x, f_r, f_\theta) = \mathbf{f_b} R/\rho U_\infty^2$. Also,the actuator disc method considers the flow as axisymmetric, therefore $\partial/\partial\theta = 0$ but $w \neq 0$. Moreover, the viscous force term remains in the momentum equations because of numerical stability in the computational process; however, the viscous force term is kept it small as possible to be treated as an inviscid flow.

Figure 2.4 shows the actual domain and the model domain. As it is seen in Figure 2.4a, the computational domain encompasses the upper half of the rotor, and the red line represents the actuator disc. In the computational domain (see Figure 2.4b), L_r and L_x are the lengths of the domain in the radial and axial directions, respectively. L_D is the position of the actuator disc.

We apply a Dirichlet boundary condition at the inlet and lateral boundaries. Besides, a Newmann condition was implemented at the outflow and symmetry line. Thus, the boundary conditions are

Symmetry axis

$$v = 0, \qquad \frac{\partial u}{\partial r} = 0, \qquad w = 0. \tag{2.59}$$

Lateral boundary

$$u = U_0, \qquad v = 0, \qquad w = 0. \tag{2.60}$$

In-flow

$$u = U_0, \qquad v = 0, \qquad w = 0. \tag{2.61}$$

Out-flow

$$\frac{\partial ur}{\partial x} = 0, \qquad \frac{\partial vr}{\partial r} = 0, \qquad \frac{\partial w}{\partial x} = 0. \tag{2.62}$$

Chapter 3

Numerical Implementation

3.1 Numerical solution of the momentum equations

This section describes how the numerical solution for the Navier-Stokes equations is implemented. Using the Finite Volume Method (FVM), the discretization process is described in rectangular bidimensional coordinates. However, the real domain is in cylindrical coordinates, but the process is similar. We assume incompressible and unsteady flow; therefore, the velocity could change over time. Using the dimensionless variables described in section 2.4, the transport equation is given as

$$\frac{\partial \mathbf{u}}{\partial t} + (\mathbf{u} \cdot \nabla)\mathbf{u} = -\nabla p + \frac{1}{Re}\nabla^2 \mathbf{u} + \mathbf{f}, \tag{3.1}$$

where Re refers to the Reynolds number, which is $Re = U_\infty L/\nu$, although this work is set to a fixed value to approach an inviscid flow; $\mathbf{f}$ represents the body force acting on the fluid, for this case, obtained by the blade element and airfoil data.

In a two-dimensional form, the Eq. 3.1 consists of two equations, but it involves three unknowns, namely, the velocity components, u and v, and the pressure, p. To achieve a closed equations system to have the same amount of equations as unknowns, we use the mass conservation equation for an incompressible fluid given as

$$\nabla \cdot \mathbf{u} = 0. \tag{3.2}$$

With this equation, the system is closed. However, there is no equation to describe the pressure or the boundary conditions for this variable. Therefore, we need to use a method to separate the velocity from the pressure. This method assumes a value for the pressure and then computing the velocities. If the convergence is not achieved, the pressure is corrected, and new velocities are calculated. These steps are repeated until convergence is reached.

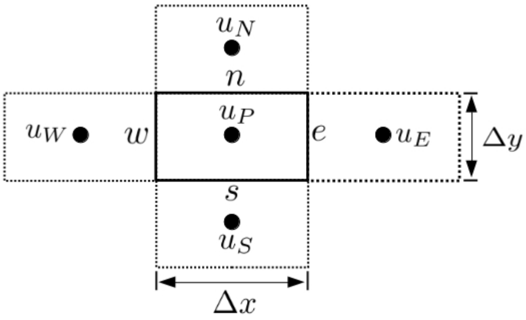

Figure 3.1: Regular grid.

The SIMPLE (Semi-Implicit Method for Pressure Linked Equations) [31] is used to solve the equations. This method uses a fourth equation that describes the pressure. The discretized equation for the u component is

$$a_P u_P = a_E u_E + a_W u_W + a_N u_N + a_S u_S + S_P, \tag{3.3}$$

using a central scheme in a regular grid (see Figure 3.1), the a_{th} coefficients of Eq. 3.3 are defined as follows

$$a_E = \frac{\Gamma_e S_e}{\Delta x} - \frac{u_e S_e}{2}, \qquad a_W = \frac{\Gamma_w S_w}{\Delta x} + \frac{u_w S_w}{2}, \tag{3.4}$$

$$a_N = \frac{\Gamma_n S_n}{\Delta y} - \frac{u_n S_n}{2}, \qquad a_S = \frac{\Gamma_s S_s}{\Delta y} + \frac{u_s S_s}{2}. \tag{3.5}$$

However, in this work, an upwind method is applied to the convective term while a central difference is kept in the diffusion term of the momentum equation. Therefore, the coefficients are given as

$$a_E = \frac{\Gamma_e S_e}{\Delta x} - \min(u_e S_e, 0), \qquad a_W = \frac{\Gamma_w S_w}{\Delta x} + \max(u_w S_w, 0), \tag{3.6}$$

$$a_N = \frac{\Gamma_n S_n}{\Delta y} - \min(u_n S_n, 0), \qquad a_S = \frac{\Gamma_s S_s}{\Delta y} + \max(u_s S_s, 0), \tag{3.7}$$

using the directions of the fluid from left to right and from bottom to top as positives. The central coefficient is

$$a_P = a_E + a_W + a_N + a_S + \frac{\Delta V}{\Delta t}, \tag{3.8}$$

$$S_P = \bar{S}_P \Delta V - \left(\frac{\partial p}{\partial x}\right)_P \Delta V + u_P^0 \frac{\Delta V}{\Delta t} = \bar{S}_P - \frac{(p_E - p_P)}{\Delta x} \Delta V + u_P^0 \frac{\Delta V}{\Delta t}. \tag{3.9}$$

Here Γ refers to the generalized diffusion coefficient, which means $\Gamma = 1/Re$; S is the surface of the cross-section of the side of the cell, V is the volume and t the time.

Using the Eq. 3.9, Eq. 3.3 can be rewritten as

$$a_P u_P = \sum_{nb} a_{nb} u_{nb} + b - (p_E - p_P) A_e, \tag{3.10}$$

with

$$b = \bar{S}_P \Delta V + u_P^0 \frac{\Delta V}{\Delta t}, \qquad A_e = \frac{\Delta V}{\Delta x} = \Delta y = S_e, \tag{3.11}$$

where the subindex nb indicates that all the close neighbors should be added.

From equation 3.10, we might notice that the velocity and pressure field must be known a priori. But one strategy to solve the problem is to assume a pressure p^*; then, we can estimate a velocity field $\mathbf{u}^*$, whose components u^* and v^* are found using the modified momentum equations as

$$a_P u_P^* = \sum_{nb} a_{nb} u_{nb}^* + b - (p_E^* - p_P^*) A_e, \tag{3.12}$$

$$a_P v_P^* = \sum_{nb} a_{nb} v_{nb}^* + b - (p_N^* - p_P^*) A_n. \tag{3.13}$$

The solution of the velocity field $\mathbf{u}^*$ might not satisfy the mass conservation; hence, in order to obtain a correct velocity field, corrections to the pressure and velocity field can be made through

$$\mathbf{u} = \mathbf{u}^* + \mathbf{u}', \qquad p = p^* + p', \tag{3.14}$$

where $\mathbf{u}'$ y p' are corrections to the velocity field and pressure, respectively. These corrections are added to the last value obtained on each iteration to achieve convergence.

Subtracting the Eq. 3.12 from Eq. 3.10 is obtained

$$a_P \underbrace{(u_P - u_P^*)}_{u'_p} = \sum_{nb} a_{nb} \underbrace{(u_{nb} - u_{nb}^*)}_{u'_{nb}} - \left(\underbrace{(p_E - p_E^*)}_{p'_E} - \underbrace{p_P - p_P^*)}_{p'_P} \right) A_e \tag{3.15}$$

or as well given by

$$a_P u'_P = \sum_{nb} a_{nb} u'_{nb} - (p'_E - p'_P) A_e. \tag{3.16}$$

By subtracting the term $\sum a_{nb} u'_P$ from both sides of Eq. 3.16 and reordering, we get

$$\left(a_P - \sum a_{nb}\right) u'_P = \sum a_{nb}(u'_{nb} - u'_P) - (p'_E - p'_P)A_e. \tag{3.17}$$

Based on the simplification made on the first term on the right-hand side, it is possible to obtain a set of different algorithms with a modified form of the SIMPLE algorithm; such as SIMPLEC, SIMPLER, or PISO. Now considering a small difference between the velocity in the center of the volume and the neighbors, we can neglect the first term on the right-hand side and order the equation to obtain the correction for the velocity u, this is given by

$$u'_P = -\frac{A_e}{a_P - \sum a_{nb}}(p'_E - p'_P) = de(p'_P - p'_E), \tag{3.18}$$

where

$$de = -\frac{A_e}{a_P - \sum a_{nb}}. \tag{3.19}$$

Applying the same for the v component, we can get

$$v'_P = -\frac{A_n}{a_P - \sum a_{nb}}(p'_N - p'_P) = dn(p'_P - p'_N), \tag{3.20}$$

with

$$dn = -\frac{A_n}{a_P - \sum a_{nb}}. \tag{3.21}$$

The consideration taken of the difference in the correction of the velocity leads to the SIMPLEC method (Semi-Implicit Method for Pressure Linked Equations Corrected). Now, remembering from Eq. 3.14 that the correction of the component u is given by $u_P = u^*_P + u'_P$ then we can incorporate the Eq. 3.18 to obtain

$$u_P = u^*_P + de(p'_P - p'_E). \tag{3.22}$$

Dealing in the same way with the component v given by $v_P = v^*_P + v'_P$ and introducing the Eq. 3.20, we can get

$$v_P = v^*_P + dn(p'_P - p'_N). \tag{3.23}$$

To correct the velocities is necessary to know the pressure field p'. Therefore, we can use the discretized continuity equation, which is

$$u_e S_e - u_w S_w + v_n S_n - v_s S_s = 0. \tag{3.24}$$

The divergence of $\mathbf{u}$ is calculated at the center of the volumes for the pressure. Thus, using a staggered grid, like the one shown in Fig. 3.2, and using the Eqs. 3.22 and 3.23, the velocities on the faces of the control volume for the pressure are computed as

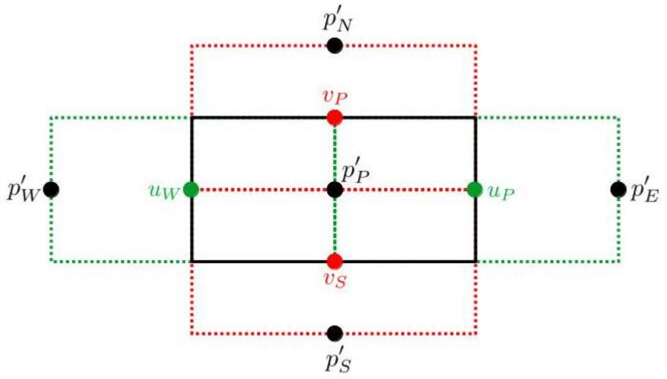

Figure 3.2: Velocities locations and pressure corrections on the staggered grid.

$$u_e = (u_P)_e = (u^*_P)_e + (de)_e(p'_P - p'_E)_e = u^*_e + (de)_e(p'_P - p'_E), \tag{3.25}$$

$$u_w = (u_P)_w = (u^*_P)_w + (de)_w(p'_P - p'_W)_w = u^*_w + (de)_w(p'_W - p'_P), \tag{3.26}$$

$$u_n = (u_P)_n = (u^*_P)_n + (dn)_n(p'_P - p'_N)_n = u^*_n + (dn)_n(p'_P - p'_N), \tag{3.27}$$

$$u_s = (u_P)_s = (u^*_P)_s + (dn)_s(p'_P - p'_N)_s = u^*_s + (dn)_s(p'_S - p'_P). \tag{3.28}$$

By replacing the upper equations and inserting them in the continuity equation and simplifying, we get

$$\begin{aligned} u^*_e S_e + (de)_e S_e p'_P - (de)_e S_e p'_E - u^*_w S_w - (de)_w S_w p'_W + (de)_w S_w p'_P \\ + v^*_n S_n + (dn)_n S_n p'_P - (dn)_n S_n p'_N - v^*_s S_s - (dn)_s S_s p'_S + (dn)_s S_s p'_P = 0, \end{aligned} \tag{3.29}$$

reordering it is obtained

$$\begin{aligned} [(de)_e S_e + (de)_w S_w + (dn)_n S_n + (dn)_s S_s] p'_P = (de)_e S_e p'_E + (de)_w S_w p'_W \\ + (dn)_n S_n p'_N + (dn)_s S_s p'_S - (u^*_e S_e - u^*_w S_w + v^*_v S_n - v^*_s S_s). \end{aligned} \tag{3.30}$$

Which could be written in the better-known way as

$$a_P p'_P = a_E p'_E + a_W p'_W + a_N p'_N + a_S p'_S + S_P, \tag{3.31}$$

where the coeffcients are

$$a_E = (de)_e S_e, \qquad a_W = (de)_w S_w, \qquad a_N = (dn)_n S_n, \qquad a_S = (dn)_s S_s, \tag{3.32}$$

$$a_P = a_E + a_W + a_N + a_S, \qquad S_P = -\nabla \cdot \mathbf{u}^* = -(u_e^* S_e - u_w^* S_w + v_n^* S_n - v_s^* S_s). \quad (3.33)$$

We obtained all the equations needed to know the pressure field as well as the velocity field. Thus, the methodology to apply the SIMPLEC method could be summarized on the next steps:

1. Assume a pressure field p^*.
2. Obtain the velocity field $\mathbf{u}$ from the pressure field assumed and using the Eqs. 3.12 and 3.13.
3. After knowing $\mathbf{u}^*$, compute the source term $(-\nabla \cdot \mathbf{u}^*)$ for the correction of the pressure and to solve the Eq. 3.31, thus, p' could be known.
4. Correct the pressure field from $p = p^* + p'$.
5. Correct the velocities from the Eqs. 3.22 and 3.23.
6. The process is repeated until convergence is achieved, so that from the solution of Eqs. 3.12 and 3.13 a velocity field with zero divergence is obtained.

3.2 Immersed boundary

3.2.1 Structure of the front

The Immersed Boundary Method [32] is a numerical method used in computational fluid dynamics. Unlike other methods, the boundary is immersed in the grid, and it does not coincide with the domain boundaries. Therefore, it is necessary to apply a special treatment to consider the boundary on the grid solution.

The front of the object consists of points, which are connected by elements (see Figure 3.3). These points contain the coordinates of the immersed object. The main purpose of the points is to describe the obstacle or the immersed object, thus transferring information between the regular grid, where the properties are computed, and the front. First, to transfer information, we must identify the closest point on the fixed grid to the given point of the front. In one dimension, we can denote the total number of grid points as NX and the length of the domain as L_x, then the grid point, which is to the left of a point at x, is given by

$$i = int(x \cdot NX/L_x). \quad (3.34)$$

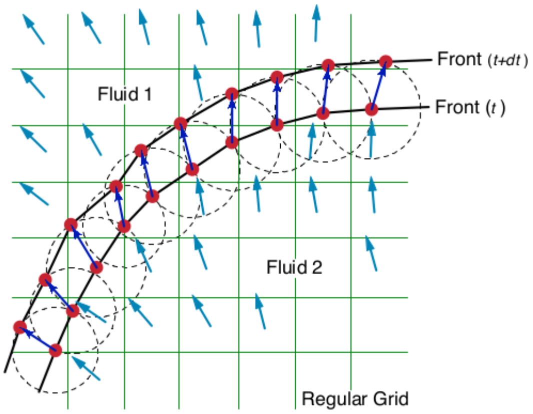

Figure 3.3: Front sketch [33].

3.2.2 Interpolating the front properties onto the fixed grid

Since the points representing the actuator surface do not coincide with any background nodes, it is necessary to use a function to interpolate the information between the fixed grid and the points. The function should gather the information on the velocity of the neighbors of a point to spread the force of the point to the nodes of the fixed grid. To convert the velocity from the fixed grid to the points, we use the expression

$$\mathbf{u}(\mathbf{X}) = \sum_{\mathbf{x}\in g_{\mathbf{x}}} \mathbf{u}(\mathbf{x})\delta(\mathbf{x}-\mathbf{X}), \tag{3.35}$$

where $g_{\mathbf{x}}$ is the set of the background cells, $\mathbf{X}$ and $\mathbf{x}$ are the coordinates of the points of the actuator disc and the centers of the fixed grid, respectively. The discrete delta function can be written as a product of one-dimensional functions, and the weight on the grid point (i, j) of the smoothing of $\mathbf{X}_p = (x_p, y_p)$ is calculated as

$$\delta(\mathbf{x}-\mathbf{X}) = d(x_p - ih_x)d(y_p - jh_y), \tag{3.36}$$

where h_x and h_y are the grid spacings in the x and y directions, respectively. We employ a weight function similar to the one developed by Peskin [34]

$$d(r) = \begin{cases} (1/4)(1+\cos(\pi r/2h), & |r| < 2h, \\ 0, & |r| \geq 2h. \end{cases} \tag{3.37}$$

The Figure 3.4 shows the geometric interpretation of the interpolation using Eq. 3.37. The point $\mathbf{x}_P$ gathers information from the nodes on the fixed grid that are around it. However, it gets only a fraction determined by the weights w, so, the node (i, j) gives a fraction $\mathrm{w}_{i,j}$ of information, the node $(i, j+1)$ gives a fraction $\mathrm{w}_{i,j+1}$, and so on. For the Eq. 3.37 it is necessary to transfer the value of the quantity from two nodes around in each direction. Therefore, in a two-dimensional domain, sixteen points of the volume grid are taken into account to give information.

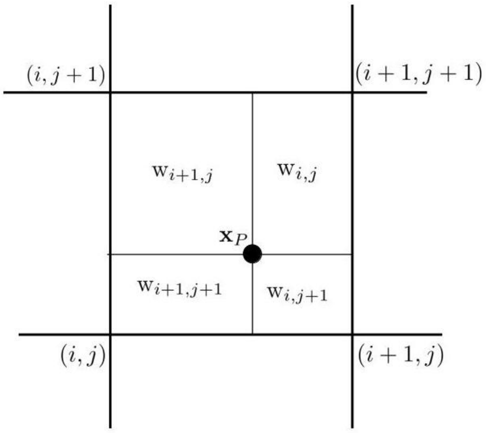

Figure 3.4: Area of weighting to interpolate properties from the fixed grid to the front.

After computing the forces acting on the actuator disc, these are spread on the fixed grid using the following equation

$$\mathbf{f}(\mathbf{x}) = \sum_{\mathbf{x} \in g_{\mathbf{x}}} \mathbf{f}(\mathbf{X}) \delta(\mathbf{x} - \mathbf{X}) \tag{3.38}$$

where $g_{\mathbf{x}}$ is the set of the actuator disc points. The same delta functions as in Eqs. 3.36 and 3.37 are employed to interpolate the forces from the points to the fixed grid.

3.3 Numerical procedure

The numerical procedure to solve the model for an actual wind turbine is shown in Figure 3.5. It depicts the steps to achieve one iteration on the flow field. The blade element theory is solved after computing the velocity field and interpolating to the points. The difference between the last value of the induction factor and the current one must be less than the error proposed, ϵ. Then the power and thrust are calculated, and the forces are applied to the Navier-Stokes equations. The time step is fixed during the simulation, namely, $dt^* = 0.005$. The cycle continues until the maximum time, t_{max}, is reached.

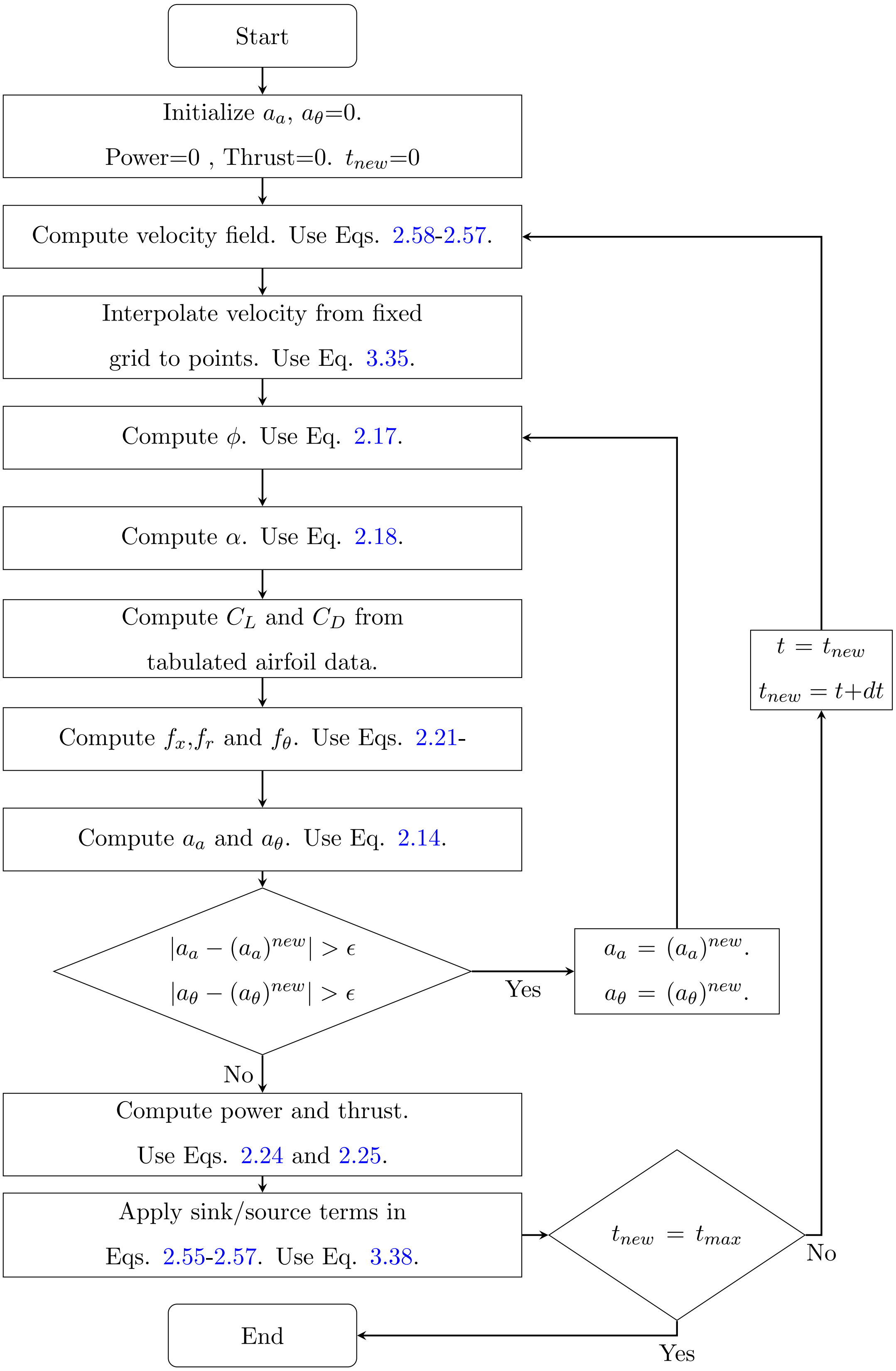
Start
Initialize a_a, a_θ=0.
Power=0 , Thrust=0. t_{new}=0
Compute velocity field. Use Eqs. 2.58-2.57.
Interpolate velocity from fixed grid to points. Use Eq. 3.35.
Compute ϕ. Use Eq. 2.17.
Compute α. Use Eq. 2.18.
Compute C_L and C_D from tabulated airfoil data.
Compute f_x,f_r and f_θ. Use Eqs. 2.21-
Compute a_a and a_θ. Use Eq. 2.14.
$|a_a - (a_a)^{new}| > \epsilon$
$|a_\theta - (a_\theta)^{new}| > \epsilon$
Yes
$a_a = (a_a)^{new}$.
$a_\theta = (a_\theta)^{new}$.
No
Compute power and thrust.
Use Eqs. 2.24 and 2.25.
Apply sink/source terms in Eqs. 2.55-2.57. Use Eq. 3.38.
$t_{new} = t_{max}$
No
$t = t_{new}$
$t_{new} = t+dt$
Yes
End

Figure 3.5: Flowchart describing the numerical steps to solve the model used.

Chapter 4

Results

This chapter presents the results of the numerical simulations for different rotor features. First, the airfoil data are obtained from the XFOIL program, and we compare them against experimental results. Thus, we expose the viability of using the XFOIL program when the experimental data are unavailable without losing reliability.

4.1 Airfoil data

Both BEM theory and CFD simulations use airfoil data to compute the rotor aerodynamic properties. However, the experimental data is not always available, and we should obtain the drag and lift coefficient from other sources. The XFOIL program is a tool to compute the airfoil characteristics. This program uses a panel method (where several points describe the airfoil shape) and the potential fluid. The XFOIL results might be used on CFD simulations, resulting in a source of information on aerodynamic tabulated data.

Later on in this work, an assessment of the baseline turbine from NREL is given. Because of that, we show a comparison of the coefficients for the S809 airfoil, which is used on the turbine. The shape of the airfoil is shown in Figure 4.1. The chord normalizes the airfoil coordinates, and we can note the large thickness, which is $t = 0.21c$. The airfoil characteristics can be found in Somers' work [35].

Using more than one profile along the blade is common in wind turbines. However, the NREL baseline wind turbine uses only one. This airfoil, S809, was specifically designed for wind turbines. Previously, most airfoils used in wind turbines were developed for airplanes. However, the purposes are significantly different between the two sets of airfoils. For wind turbines, a high lift-to-drag ratio is wanted to improve the aerodynamic performance. Also, a high relative thickness helps to reduce blade weight. The drag should remain low over a wide range of lift coefficients. On the other hand, according to Timmer and Bak [36], the addition of roughness to the leading edge must have little influence on the boundary-layer development.

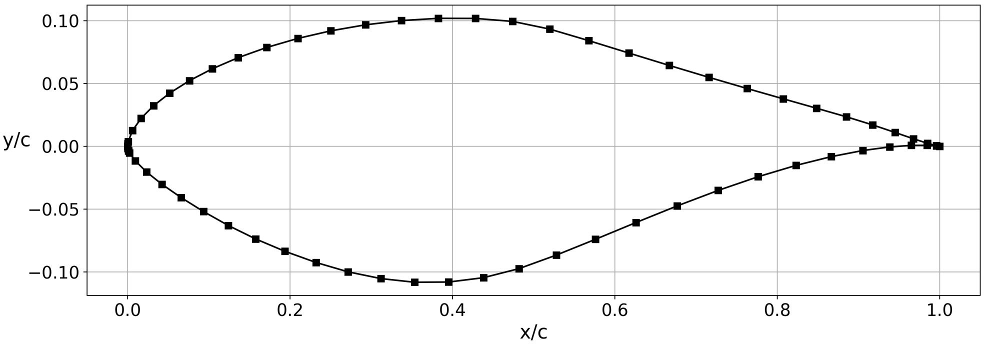

Figure 4.1: S809 airfoil coordinates.

The lift and drag coefficients are presented in Figure 4.2. Three different sources are displayed; the experimental data (found in Hand's work [37]) from Delft University of Technology (DUT) and Ohio State University (OSU), and an approximation from XFOIL using as interface QBlade program. The angles of attack range from -5 to 15 degrees for $Re = 1,000,000$. The Reynolds number was selected according to the one expected on the simulation results. We can see a good prediction made by XFOIL, where the lifting behavior is similar for all data. The drag coefficient has a minor difference after 10 degrees for the DUT experimental data; however, it agrees in all the remaining ranges.

For the S809 airfoil, the airfoil data obtained by XFOIL agree with the experimental sets. Therefore, the XFOIL set is used for the calculations in the next sections, extrap-

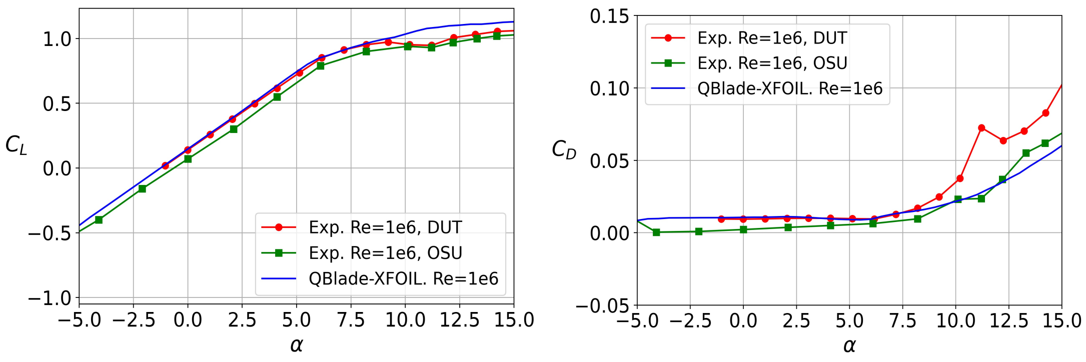

(a) Lift coefficient.

(b) Drag coefficient.

Figure 4.2: Lift (a) and drag (b) coefficients for S809 airfoil.

olating them through a Montgomerie method [38]. This data set is found in Appendix A.1. When the whole empirical airfoil data are not available, this procedure can solve the lack of information.

4.2 The constant loaded rotor disc

We imposed a uniform constant force on the whole rotor surface in an one-dimensional analysis. It is an idealized case and comes from the one-dimensional momentum theory already presented, in which the main result is that the maximum power is obtained for $a_a = 1/3$, where the thrust and power coefficients can be computed as $C_T = 4a_a(1-a_a)$ and $C_P = 4a_a(1-a_a)^2$, respectively. To validate this theory, several values for a_a are given and the thrust imposed is calculated by Eq. 2.10. The force is implemented in a two-dimensional domain following the methodology exposed in chapter 3.

4.2.1 Numerical tests

Several tests were made for the loaded rotor ($C_T = 0.8$) case to analyze the influence of the domain size and grid resolution on the aerodynamic performance results. The latter will help us to optimize and save computational resources. The domain tests are divided in two cases. In the first one, we vary the radial length and fix the axial length in $L_x = 13R$. This value is chosen to have enough space behind the rotor, so the wake can develop. In the second case, taking advantage of the previous result, the radial length is fixed and the axial length changes.

The number of control volumes is modified in every test to keep the thickness of the grid constant regardless of the length. Thus, 15 and 20 cells are used per radius in the axial and radial directions, respectively. This results in a cell with sides $dx = 0.06$ and $dy = 0.05$. Also, the dimensionless time, t^*, is fixed $t^* = 100$. The rotor is located three radii downstream from the inlet, and two points that describe the rotor are set per cell.

We calculate the averaged axial factor, $\bar{a}_a$, along the blade to compare the results. This computation is made by taking the sum of the axial factor of each section and dividing it by the total number of sections. Figure 4.3 shows the averaged axial factor along the blade for several lengths in the radial direction keeping $L_x = 13R$. For four radii, the axial factor is out of the range of numerical stability. The difference between the values obtained begins to decrease after six radii. From this point, the results oscillate from 0.34 to 0.36 without reaching a fixed value. Therefore, we can assume that, since $L_r = 6R$, any of the radial lengths shown lead to similar results that remain in the

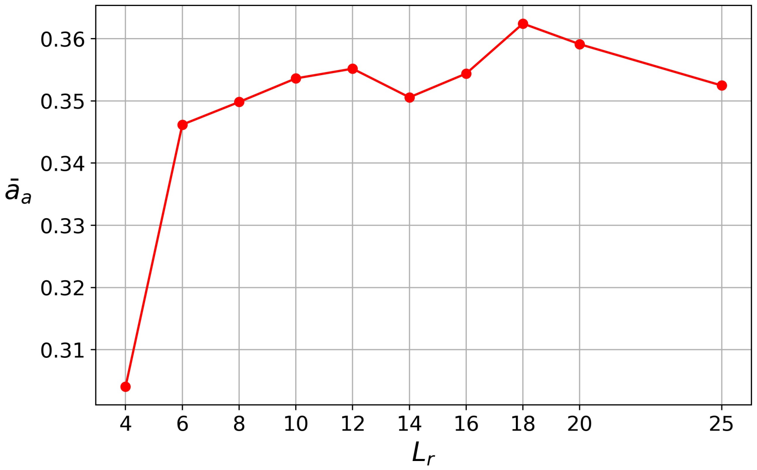

Figure 4.3: Averaged axial factor for different radial lengths

range of stability.

Table 4.1 depicts the averaged axial factors and the relative error, ϵ, of each one against $L_r = 25R$, which is the longest length. The relative error found for $L_r > 6R$ is less than 2 %. Also, we can see a small variation, less than one percent, of the factor while we increase the radial length, except for 18 and 20 radii. It is notorious that the axial value oscillates between 0.34 and 0.36. Therefore, we decided to fix the radial length to $L_r = 6R$ for all the following simulations since $\epsilon < 2$ % is within the range where the axial value varies. Thus, we can guarantee less computational time.

Table 4.1: Averaged axial factor and relative error, ϵ, for several L_r.

$L_r[R]$	**Averaged axial factor**	ϵ [%]
25	0.35	0
20	0.359	1.884
18	0.362	2.824
16	0.354	0.545
14	0.351	0.539
12	0.355	0.768
10	0.354	0.325
8	0.350	0.751
6	0.346	1.784
4	0.304	13.737

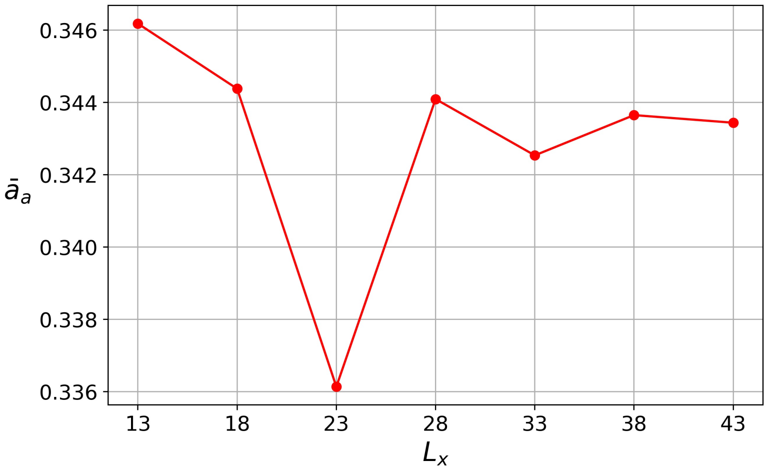

Figure 4.4: Averaged axial factor for different axial lengths

Figure 4.4 displays the averaged axial factor for several axial lengths. As a conclusion of the previous test, the simulations were made keeping $L_r = 6R$. The variation for the radius configurations is small, namely, $0.342 < \bar{a}_a < 0.348$. Only an important variation out of this range is seen for $L_x = 23$. However, its relative error is just 2.12% against the averaged axial factor for $L_x = 43R$, as Table 4.2 shows. Most configurations of the axial lengths have a minor impact on the averaged axial factor, remaining around $\bar{a}_a = 0.34$.

In Table 4.2 the most relative errors are less than one percent against the largest axial length. Hence, the axial length is set as $L_x = 13$, which means there are ten radii between the rotor and the outlet. So, we keep the accuracy and reduce the computational time.

Table 4.2: Averaged axial factor and relative error, ϵ, for several L_x.

$L_x[R]$	**Averaged axial factor**	ϵ [%]
43	0.3434	0
38	0.3437	0.0613
33	0.3425	0.2629
28	0.3441	0.1906
23	0.3361	2.1263
18	0.3444	0.2739
13	0.3462	0.7984

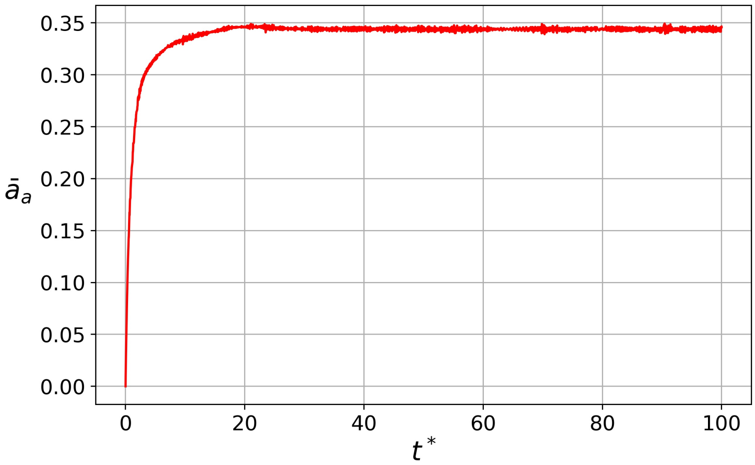

Figure 4.5: Averaged axial factor through the dimensionless time for $C_T = 0.8$.

From the above numerical tests results, the simulations in this work have been made in a domain with 13 radii in the axial direction and six radii in the radial direction. The grid points are 200 and 120 in the axial and radial directions, respectively. The rotor is set at 3 radii from the inlet and is built by 40 points, corresponding to the points used on the immersed boundary method. Thus, there are two rotor points for each cell in the fixed grid. As it is commented by Sørensen et al. [39], the Reynolds number has a minor effect on the results of this kind of model. Thus, it is set $Re = 10000$ for all the simulations.

To know when numerical stability is reached, the averaged axial factor for the rotor was computed and plotted through time. Figure 4.5 displays the averaged axial factor along the time. In the first time steps the value increases up to nearly $\bar{a}_a = 0.35$, where after $t^* = 20$, it remains almost constant with some negligible variations. Since we evaluate a flow that changes with time, the first steps represent the flow entering the domain, moving to the rotor, and passing through it. After the flow travels all the domains, it tends to a stationary state, where the averaged axial factor is reached. Up to $t^* = 50$, we can see the transition of the flow field to a steady-state without expending a large computational time.

4.2.2 Numerical results

Here, we present the results from one-dimensional theory and the two-dimensional CFD model results considering the axial and radial directions but no wake rotation. A constant load is imposed on the CFD model using $C_T = 0.4$, which results in an axial

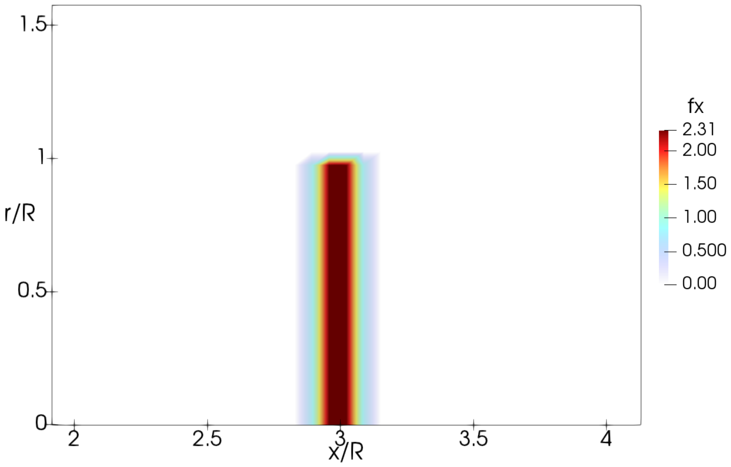

Figure 4.6: Dimensionless axial force for $C_T = 0.4$.

factor $a_a = 0.1127$. The dimensionless force that perturbs the velocity field is shown in Figure 4.6. The rotor is set at $x/R = 3$, and because of the implementation of the smooth function in the immersed boundary method to distribute the force on the fixed grid, there is a force gradient around the rotor location. The maximum force occurs at the rotor plane location, but the flow can feel the presence in the space around it.

Figure 4.7 shows the axial velocity and the axial interference factor throughout the radius. The axial velocity seems constant up to near the rotor's tip, where it decreases (see Figure 4.7a). Thrust coefficients lower than 0.4 reach constant values for both variables. When the thrust coefficient is greater than 0.4, the decrease in axial velocity

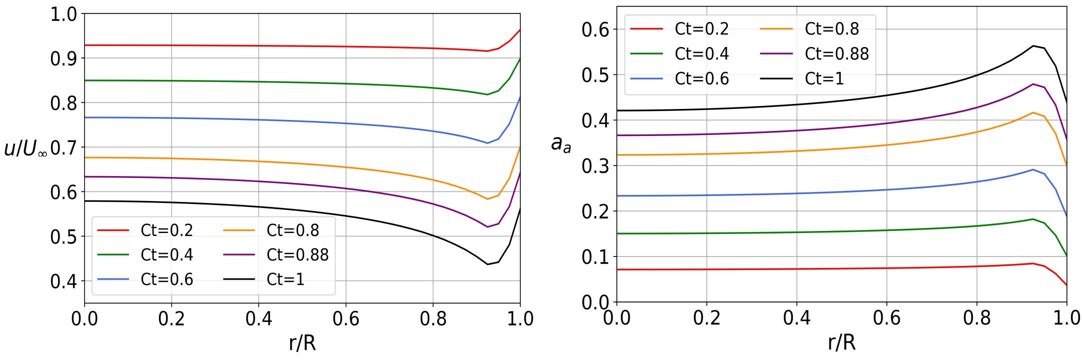

(a) Axial velocity.

(b) Axial factor.

Figure 4.7: Axial velocity (a) and axial factor (b) along the radius for several thrust coefficients.

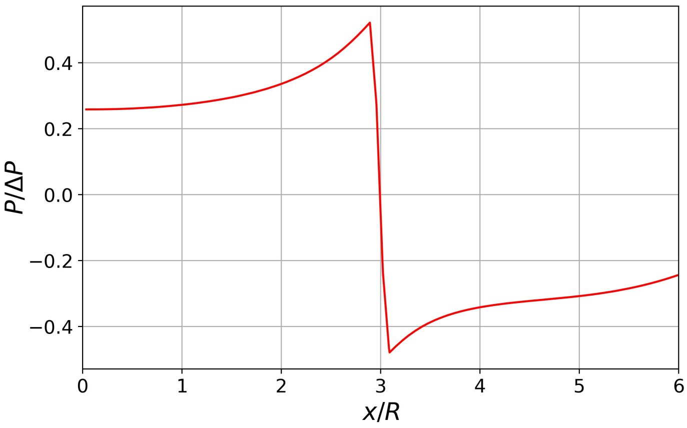

Figure 4.8: Pressure along the axial direction for r/R=0.5.

and interference factor at the tip is more notorious. Figure 4.7b shows that the axial interference factor is greater at the edge of the rotor, which means that despite imposing a constant load, the velocity is not the same in the radial direction on the rotor.

Figure 4.8 shows the normalized pressure jump at rotor position, $x/R = 3$. This figure helps to illustrate the actuator disc method, which introduces a pressure discontinuity that acts against the flow and imposes a force that decelerates the flow. The pressure decreases some radii from the front and attains a greater value right where the rotor is. Since a pressure jump is at the disc position, the axial and radial velocity must change in the front and behind the rotor. Some radii downstream, the pressure tends to recover.

Figure 4.9 displays the axial and radial velocity upstream to downstream at $r/R = 0.5$ for the constant loaded rotor. The axial velocity begins to decrease almost two radii in front of the rotor and continues reducing downstream the rotor (see Figure 4.9a). Thus, we can see that the perturbation caused by the rotor impacts the flow field some radii around and, even behind the rotor, the flow slows down. Also, Figure 4.9b depicts that the radial velocity is affected some radii around the rotor, reaching the maximum value at the rotor location, even though the one-dimensional momentum theory does not include the radial velocity inside its analysis. However, the radial velocity is modified on the flow field using the CFD model. Because of the linkage of the velocity variables on the Navier-Stokes equations, the change of the radial velocity can affect the velocities in other directions. Therefore, this can impact the rotor performance.

The flow field is shown in Figure 4.10. We can see the velocity transition around one rotor radius, reaching the smallest velocity behind it. The flow is accelerated beyond the tip, but it tends to recover some radius far away from the rotor. Behind the rotor, the velocity decreases up to 0.676, which agrees with the axial factor ($a = 0.173$) found on the most rotor spanwise and shown in Figure 4.7.

Figure 4.11 depicts the tip vorticity and the streamlines for $C_T = 0.4$. Positive vorticity values indicate a clockwise rotation, and negative values indicate counter-clockwise rotation. Tip vorticity is shed from the edge of the actuator disc, and it tends to dissipate and expand downstream (see Figure 4.11a). The vortex generation at the tip is because of the velocity change at the tip. Near the edge, the flow tends to incorporate to recover the upstream velocity driving a greater velocity gradient in this region. Thus, the change of the axial velocity in the radial direction prevails. Therefore, the flow starts to rotate. Figure 4.11b shows the wake expansion occurring behind the rotor, where the velocity increases to the sides of the rotor. The wake expansion shown agrees with the one-dimensional analysis presented previously. The general behavior of the wake is to have a larger expansion while the load grows.

In summary, the contrast between the one-dimensional momentum theory and the CFD model is presented. The drop of the pressure on the rotor plane agrees with the theory. However, the CFD model does not achieve the constant axial factor on the rotor plane. At the tip, a decrease in the axial velocity is shown. This decrease induces a velocity gradient and a vortex shed on the wake. Also, contrary to the assumptions of the one-dimensional theory, the CFD model shows a change in the radial velocity on the rotor plane, which can affect the axial velocity on the rotor plane because of the connection of both velocities in the Navier-Stokes equations.

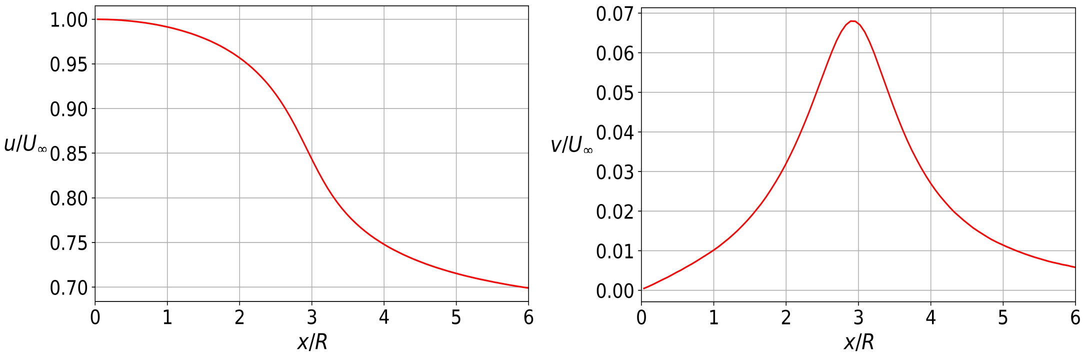

(a) Axial velocity.

(b) Radial velocity.

Figure 4.9: Axial (a) and radial (b) velocity upstream and downstream for $C_T = 0.4$ at $r/R = 0.5$.

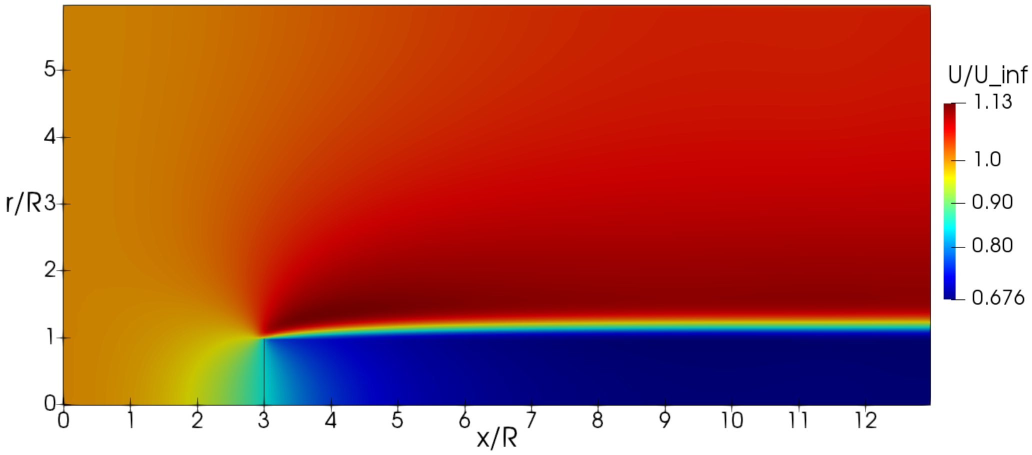

Figure 4.10: Velocity field for $C_T = 0.4$. The disc is represented by a straight line.

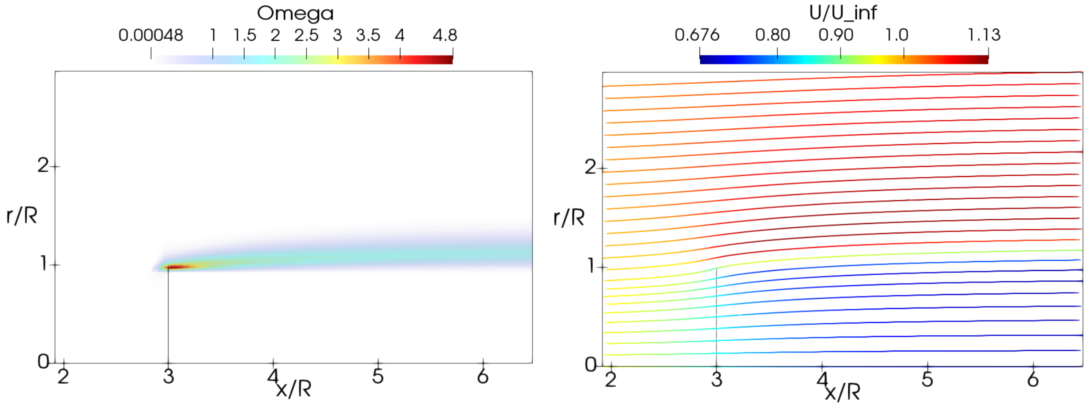

(a) Tip vorticity.

(b) Streamlines.

Figure 4.11: Tip vorticity (a) and streamlines (b) for a constant loaded rotor disc with $C_T = 0.4$. The disc is represented by a straight line.

4.3 Simulation on NREL baseline wind turbine

The implementation of the numerical code was made using the NREL baseline turbine, which is described by Giguere and Selig [40]. This turbine is stall regulated with three blades of 5.03 m each one. The blade sections consist of NREL S809 airfoil, and the rotor rotates at 72 RPM. The blade was divided into 40 sections and its geometry is found in Appendix A.2. For all the simulations, $Re = 10000$ was set. We obtained the forces and the aerodynamic properties following the methodology exposed in Section 2.2.

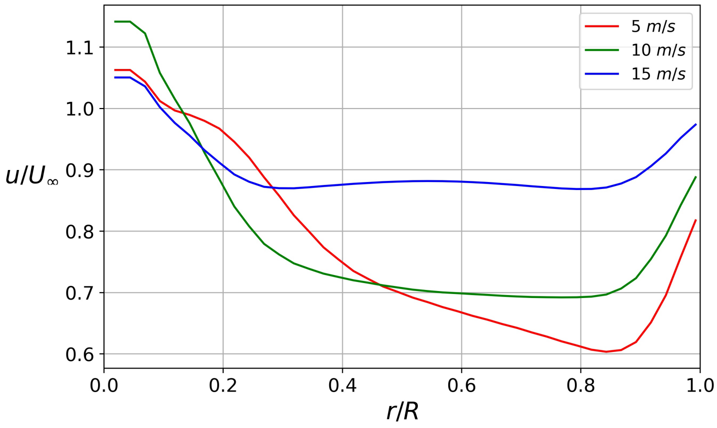

Figure 4.12: Axial velocity for several inflow values.

Various simulations were conducted to analyze the rotor performance at different inflow velocities. Figure 4.12 depicts the normalized axial velocity throughout the rotor for several inflow values. For all inflow values, the axial velocity increases at the center of the rotor, which might occur because of the hub correction; this will be discussed later in this work. The smallest inflow value results in small values along with the rotor. For $U_\infty = 15\ m/s$ the velocity tends to remains constant after $r/R = 0.2$, the same happens for $U_\infty = 10\ m/s$ after $r/R = 0.4$. For all the inflow values, the axial velocities start to recover after $r/R = 0.8$. Thus, for higher incoming values, the rotor plane's normalized axial velocities are greater, resulting in lower axial induction factors.

The radial velocity along the rotor is shown in Figure 4.13. The general behavior of

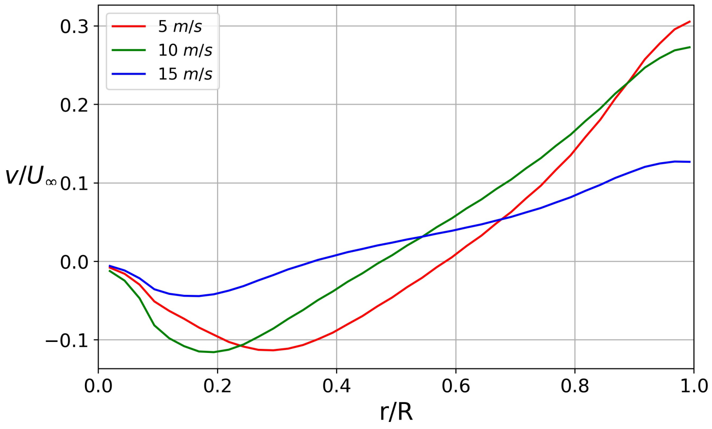

Figure 4.13: Radial velocity for several inflow values.

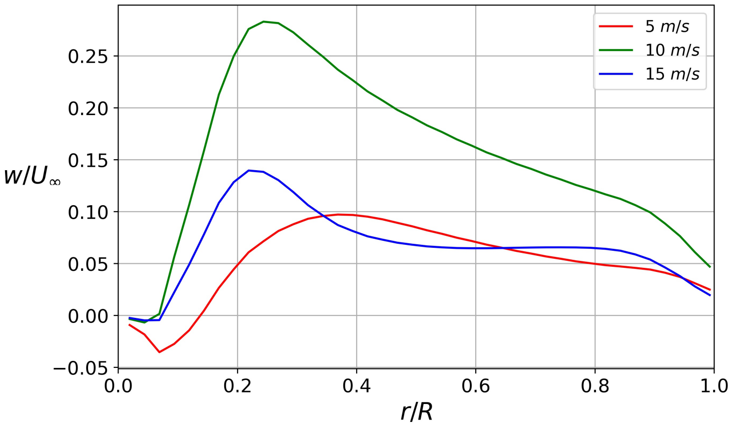

Figure 4.14: Tangential velocity for several inflow values.

the velocity is to take negative values near the root of the rotor and increase up to the tip. The higher the inflow velocity, the lower the slope of the curve. For all the upstream velocities, the radial velocity changes its sign around the mid-plane of the rotor. The latter indicates that the wake expands in both directions but faster in the positive radial direction.

Figure 4.14 illustrates the tangential velocity for several inflow values. For $U_\infty = 5$ m/s, negative values are near the root and the maximum tangential velocity is reached close to $r/R = 0.4$. For $U_\infty = 15$ m/s, the tangential velocity remains constant from $r/R = 0.5$ to $r/R = 0.8$. The maximum velocity is attained close to $r/R = 0.2$, which corresponds to the point where the lifting surface of the rotor starts. After $r/R = 0.8$, the tangential velocity decreases to recover its original value. Like the radial velocity, some negative values are obtained at the center of the rotor plane; it is notorious for the smallest velocity, which might affect the rotor's power generation since it depends on the tangential velocities reached throughout the blade.

The rotor aerodynamic performance is described by the axial and tangential factors, which are shown in Figure 4.15. This figure shows both interference factors at different inflow conditions: 5, 10, and 15 m/s. In Figure 4.15a, it is noted that the axial factor remains constant for $U_\infty \geq 10$ m/s in some sections on the rotor. For the highest inflow value, from $r/R = 0.2$ to $r/R = 0.8$, the axial factor is constant taking a value around $a = 0.1$. For $U_\infty = 10$ m/s, the constant factor is reached after $r/R = 0.4$. When the inflow velocity is 5 m/s, different behavior is found. The axial factor increases up to a maximum value, after which it decreases. All the behaviors coincide with a decrease in the same point, namely, after $r/R = 0.8$. The negative values of the axial factor ($a_a = 1 - u_R/U_\infty$) near the root indicate that the axial velocity on the rotor plane is increasing, as well as the reduction close to the tip is due to the flow trying to recover its original velocity. This agrees with the exposed in Figure 4.12. The differences found

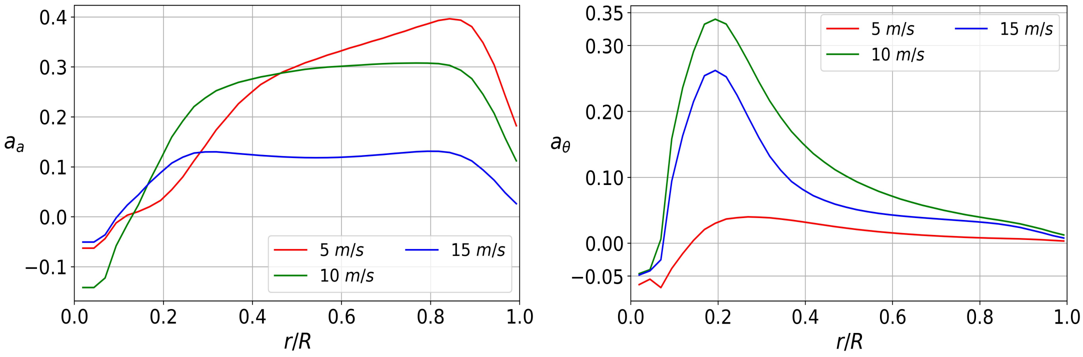

(a) Axial factor.

(b) Tangential factor.

Figure 4.15: Axial (a) and tangential (a) factor along the rotor.

for the three cases are because the velocities occurring at the rotor plane are greater for higher inflow values. Thus, the term u_R/U_∞ in the axial factor equation increases while the inflow velocity does.

Figure 4.15b shows that the tangential factor, for 10 and 15 m/s, reaches the maximum at r/R = 0.2 and decreases to about zero at the tip. However, for $U_\infty = 5\ m/s$, the increment of the tangential factor is not as much as the previous ones. Moreover, for this small inflow value, there is a very lower tangential velocity across the rotor and the peak is small. For all the inflow values, the tangential factor is negative in the first sections, which leads to negative tangential velocities, as it is exposed in Figure 4.14.

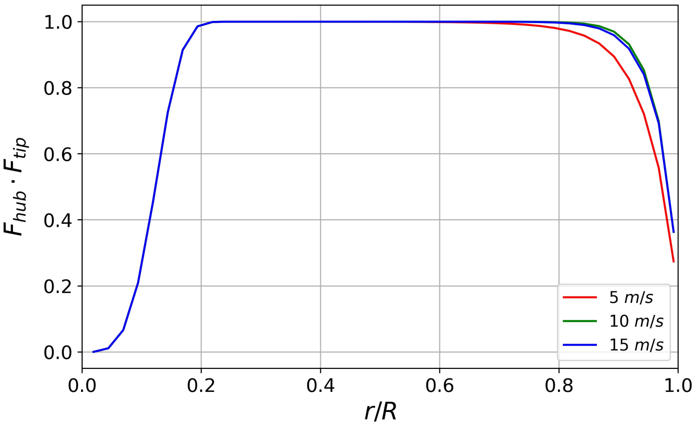

Figure 4.16: Corrections product.

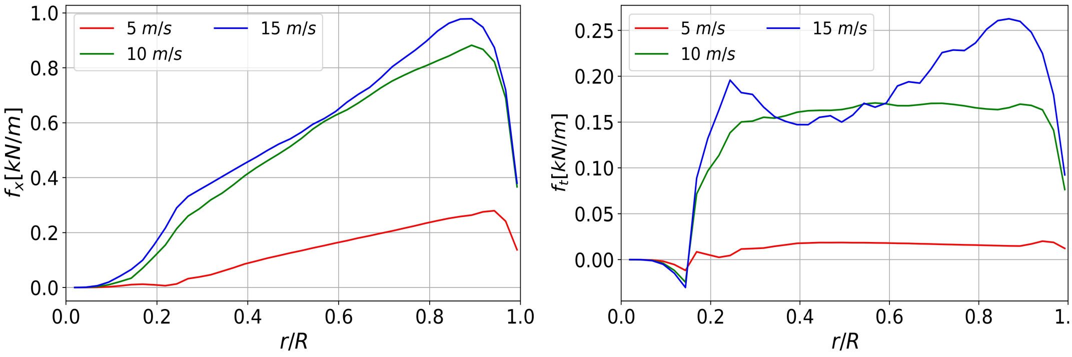

(a) Axial force.

(b) Tangential force.

Figure 4.17: Axial (a) and tangential (b) forces along the rotor.

The tip and hub corrections greatly influence the force distribution on the blades. The tip and hub corrections used in the present research work are the Eqs. 2.44 and 2.47, respectively. As we can see in Figure 4.16, the hub correction reduces the forces to zero on the center of the rotor. Besides, the force drops at the tip because of the tip correction. In Eq. 2.44 it is clear that the value of the tip corrections depends on the flow angle, ϕ, which changes with the velocity. Therefore, we can appreciate a different form of tip correction curves for every incoming velocity.

The axial and tangential forces per blade span are given in Figure 4.17 for inflow values of 5, 10 and 15 m/s. The axial and tangential forces reach greater values when the inflow velocity increases. Therefore, it might generate more power. Figure 4.17a depicts that the axial forces for 10 and 15 m/s cases are close, achieving a maximum after 80% of the radius. Near the tip, both forces go down because the pressure on this region tends to be equal at the upper and lower surface of the wind turbine blade; this results from tip correction implementation. The tangential force is negative for all the cases near the root and goes up to where the lifting surface of the rotor blade starts (see Figure 4.17b). For an entry of 10 m/s the tangential force is constant roughly from $r/R = 0.3$ to $r/R = 0.9$, after this point it tends to reduce. The tangential force produced by an inflow of 15 m/s shows a great variation throughout the rotor, having a decrease where the force commonly is constant; however, the peak of the force after $r/R = 0.8$ is noticeably greater than for the other inflow values.

Following the formulation exposed in Section 2.3, a BEM method computational code was made in order to compare results against the actuator disc model presented in the current research thesis. BEM theory is widely used in wind turbine design and the description of the forces acting on the rotor. CFD simulations and BEM theory are the two most popular approaches to describe wind turbine performance. Figure 4.18 depicts the thrust and torque along the rotor. We can see how thrust and torque

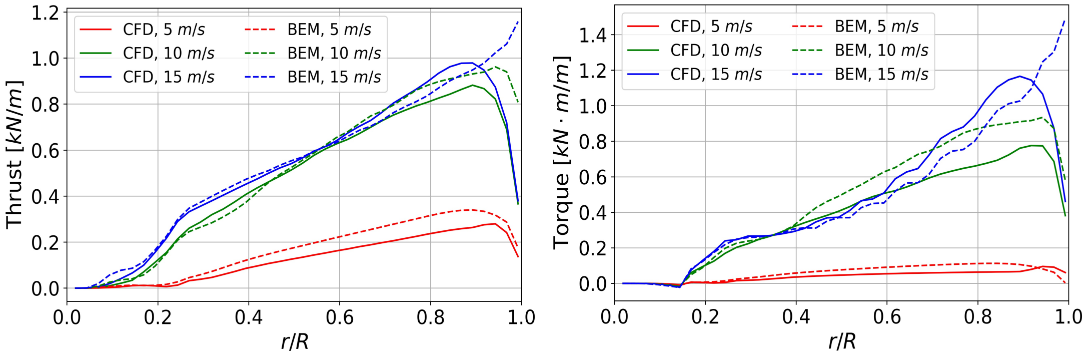

(a) Thrust. **(b)** Torque.

Figure 4.18: Thrust (a) and torque (b) calculated by BEM and CFD at different inflow velocities.

increase with a higher inflow velocity. The BEM theory follows the trend given by the CFD simulations. However, almost all the cases (except $U_\infty = 15\ m/s$) overpredict the load on the rotor, as the dashed lines show. In Figure 4.18a, we can see that the thrust for any inflow value tends to increase throughout the rotor. Near the tip, it decreases because of the tip correction. For $U_\infty = 15\ m/s$, both thrust predictions agree very well; however, BEM theory seems incapable of incorporating the load drop on edge.

Power is proportional to torque, so we can notice that the most power is generated outboard. As shown in Figure 4.18b, near the center the thrust is almost zero. Thus, no power is generated, which indicates that incorporating the hub correction has more impact on the flow field than on the turbine performance. For the lowest inflow value, the torque is small, which results in a smaller generated power amount. For $U_\infty = 10$ m/s, BEM theory predicts a larger torque over the rotor after $r/R = 0.4$. When the $U_\infty = 15\ m/s$, BEM theory predicts a smaller torque and does not consider the decrease close to the tip. For greater upstream velocities, the BEM theory can not reproduce the tip effect, resulting in an overprediction of the output power produced in this region.

To evaluate the accuracy of the results, in Figure 4.19 the power and thrust are given by several inflow velocities. The results from BEM theory and CFD are compared to experimental data. The CFD computations seem to agree better with the experiments than the BEM theory for both graphs. The power computed by CFD follows close to the actual power curve up to $U_\infty = 12.5\ m/s$, where the power predicted is higher than the measured. The power calculated using the BEM theory behaves more linearly, although, at $U_\infty = 12.5\ m/s$, it starts to decrease just as the CFD results do. In order to compare the results, a polynomial function was fitted to the experimental data, thus, obtaining the results for the same velocities used in the simulations. After that, we can compute the relative error, ϵ, between the three data sets for each velocity value. For

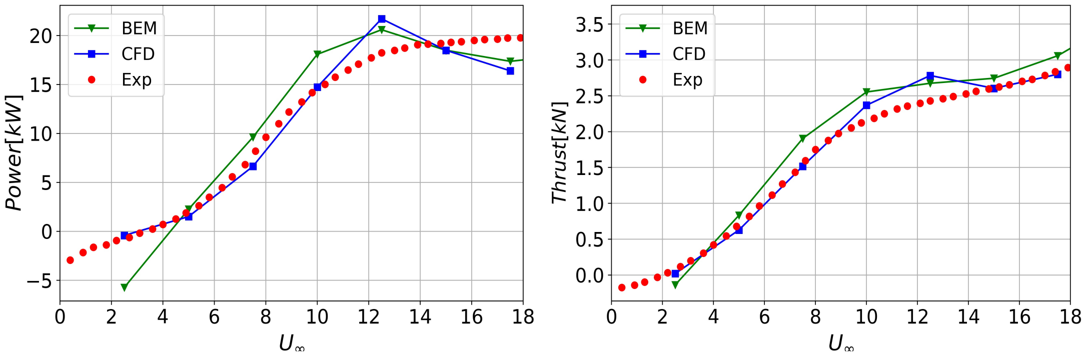

(a) Power.

(b) Thrust.

Figure 4.19: Power (a) and thrust (b) calculated by CFD and BEM theory, compared with experimental data.

$U_\infty = 2.5\ m/s$, in the cut-in speed region ($0 < U_\infty \leq 3$), the relative error by CFD is 43.73 %, whilst by BEM method is 674.80 %. In this region, the BEM method predicts smaller angles of attack than the CFD model. Therefore, minor power production is obtained. Within the transition zone ($3 < U_\infty \leq 14$), for $U_\infty = 7.5\ m/s$, $\epsilon = 16.37$ for CFD computation and $\epsilon = 21.18$ for BEM method. Finally, in the rated output region ($14 < U_\infty \leq 18$), for a wind speed $U_\infty = 15\ m/s$, the relative errors are 3.94 % and 3.94 %, by CFD and BEM results, respectively. We can conclude that the relative error reached by CFD computations is lower than the BEM results for several points in each region of the power curve.

The thrust predicted by CFD follows closer to the thrust curve than the BEM theory does. The load is greater for large inflow velocities, and both methods properly capture this. However, the results are overpredicted even if the BEM theory can drive the thrust correctly. The relative error, ϵ, was calculated for the thrust values. In the cut-in speed zone, for $U_\infty = 2.5\ m/s$, the thrust predicted by CFD achieves a relative error equals to $\epsilon = 74.54$, whilst the BEM method gets an error $\epsilon = 266.74$. For $U_\infty = 7.5$ m/s, within the transition zone, the CFD computation results $\epsilon = 2.94$ and the BEM method results $\epsilon = 21.76$. In the rated output region, for a wind speed $U_\infty = 15\ m/s$, $\epsilon = 0.41$ is obtained using CFD model and $\epsilon = 4.96$ using the BEM theory. Thus, in general, we can conclude that the CFD model proposed gives better predictions of the thrust than the well-known BEM theory.

The power predicted at high velocities does not completely agree with the experimental measurements. Even the numerical models reach a local maximum around $U_\infty = 12.5$ m/s. Different reasons can cause this disagreement, such as the difference between the coefficients given by XFOIL and the experimental ones. Also, in the experiments, there might be other uncertainties like the instrumentation system's accuracy or the support

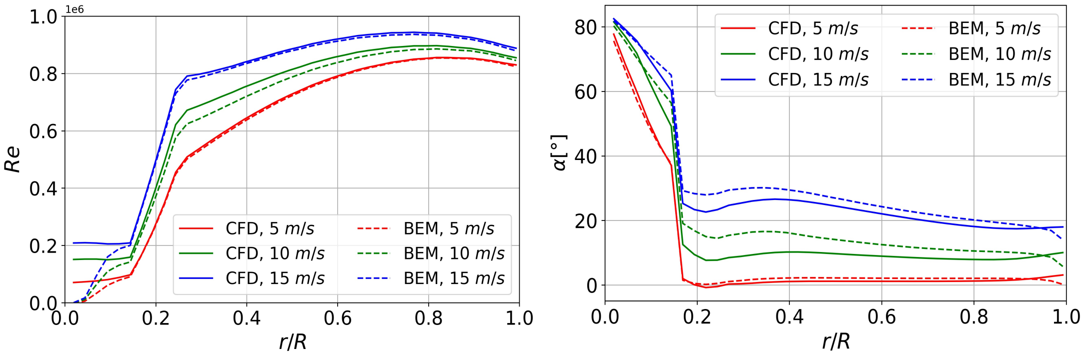

(a) Reynolds number.

(b) Attack angle.

Figure 4.20: Reynolds number (a) and attack angle (b) calculated by BEM and CFD at different inflow velocities.

structure's effect. Besides, this inaccuracy could be due to high Reynolds numbers and the attack angles occurring on the blades. In order to understand the discrepancy, Figure 4.20 illustrates the Reynolds numbers and the attack angles occurring on the rotor in the radial direction calculated by the CFD model and the BEM theory. Both methods tend to coincide. The Reynolds number grows with the inflow velocity. The angle of attack is almost constant after $r/R = 0.2$ for all the upstream velocities, and it increases with the incoming velocity. In general, when the airfoils are under a large Reynolds number and have high attack angles, the flow on the upper surface starts to detach, driving to the stall region, which results in a turbulent flow that affects the wind turbine rotor performance. Therefore, it is important to have reliable airfoil data incorporating the turbulent effect. Moreover, the result errors for large inflow velocities could be due to the lack of a turbulent term in the model. It would be necessary to explore the application of a turbulent model to predict this region where the dissipation can be more important than the current flow.

In conclusion, the CFD model can predict the loads and interference factors throughout the rotor. The velocities behavior on the rotor varies depending on the incoming speeds. Besides, the axial loads tend to increase to the tip and then fall because of tip correction. The tangential loads remain constant on the most rotor for $U_0 \leq 10$ and decrease at the tip. In the cut-in speed and the transition zone, the power and thrust predicted by CFD have a smaller error than the BEM method results . In the rated output region, the power error resulting from the CFD model becomes higher.

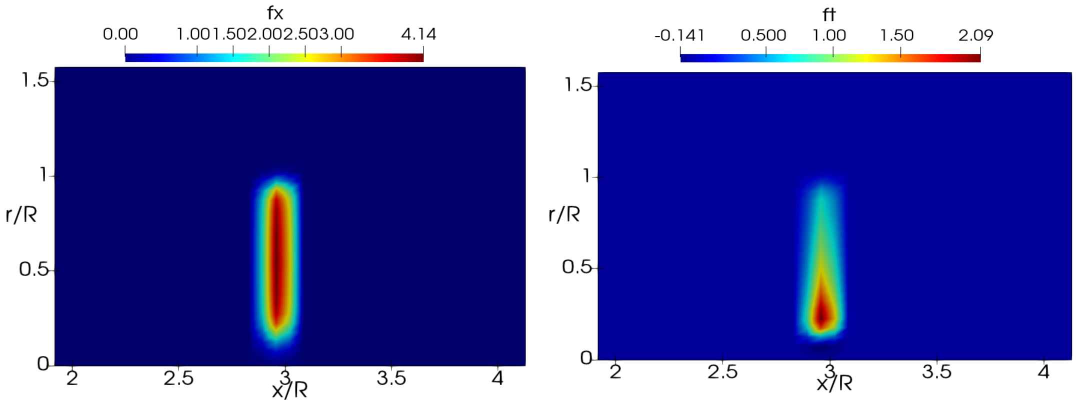

(a) Axial dimensionless force.

(b) Tangential dimensionless force.

Figure 4.21: Axial (a) and tangential (b) dimensionless forces imposed for the baseline turbine for $U_\infty = 10\ m/s$.

4.3.1 Flow field properties

One of the advantages of applying the CFD analysis is to visualize the flow around the rotor, the wake expansion, and the recovered velocity. Here, we present some flow field properties for $U_\infty = 10\ m/s$ as a general view of the flow. To show the difference in the force imposed on the flow field considering a constant load on the rotor and an actual wind turbine rotor aerodynamics. Figure 4.21 displays the dimensionless forces in the axial and tangential directions. We can see that no force is imposed near the root of the rotor in both directions because of the hub correction. The axial force seems to be constant from where the lifting surface on the rotor begins up to the tip (see Figure 4.21a). The implementation of the hub correction constrains the axial force to be zero on the center of the rotor, which could not be completely correct since the hub presence must impose a force on the flow. Moreover, the tangential force changes along the radial direction. The maximum is obtained on the inboard sections, and then it decreases as it gets closer to the tip (see Figure 4.21b). We must highlight that negative values of the tangential forces are achieved near the root, which might be produced because of using a cylinder on the representation of the hub and the hub correction itself.

The complete velocity field for the whole domain is shown in Figure 4.22. The rotor is set at $x = 3R$, and the free stream normalizes the velocity. We can see how the velocity decreases about one radius in front of the rotor, and then a velocity transition zone begins up to the rotor plane. This zone consists of a velocity gradient because of the forces imposed on the rotor plane. The shape of this region depends on the way to interpolate the forces occurring on the rotor, for this case given by Eq. 3.37. The hub correction is more relevant near the center at $r/R = 0$; thus, the forces take a small value on this area. It causes a gap between the symmetry axis and the first force imposed, for which the flow tries to pass, increasing its velocity. After this zone, the force starts to be imposed, and the flow is decelerated. The velocity decreases throughout the rotor to the tip, where a fast transition zone occurs. Off the rotor, the flow is accelerated in the radial direction, and it tries slowly to recover its original value while it gets away from the rotor. In this model, the presence of the rotor can disturb the flow of several radii around, which indicates that if more wind turbines were behind, their performance would be affected.

The streamlines for $U_\infty = 10\ m/s$ are displayed in Figure 4.23. It is easy to note the wake expansion behind the rotor and the flow increment above it. Close to the rotor plane, the streamlines change their direction, becoming more sloped on the edge.

We examine the vorticity field in Figure 4.24. We can see the opposite sign of the vorticity within the inner root layer and outer tip layer. The increment in velocity near the symmetry axis line, as shown in 4.22, results in a vortex shed in the inner region. The tip sheds a second vortex, and it expands and gets smoother while it travels behind the rotor. The dissipation of the vorticity is not completely captured in the model presented in this work because of the lack of a turbulent term; however, the most relevant phenomenon is predicted as the tip vortex.

The velocity must be recovered some radii downstream in an actual real flow passing a wind turbine rotor. The latter has an important impact on the performance of the turbines located inside the wake of another rotor. To know how the flow recovery is, Figure 4.25 shows the distribution of the axial, radial, and tangential velocities at various downstream locations using three different inflow values. The axial velocity along the rotor is notably constant for $U_\infty = 15\ m/s$, but this constant value is lost

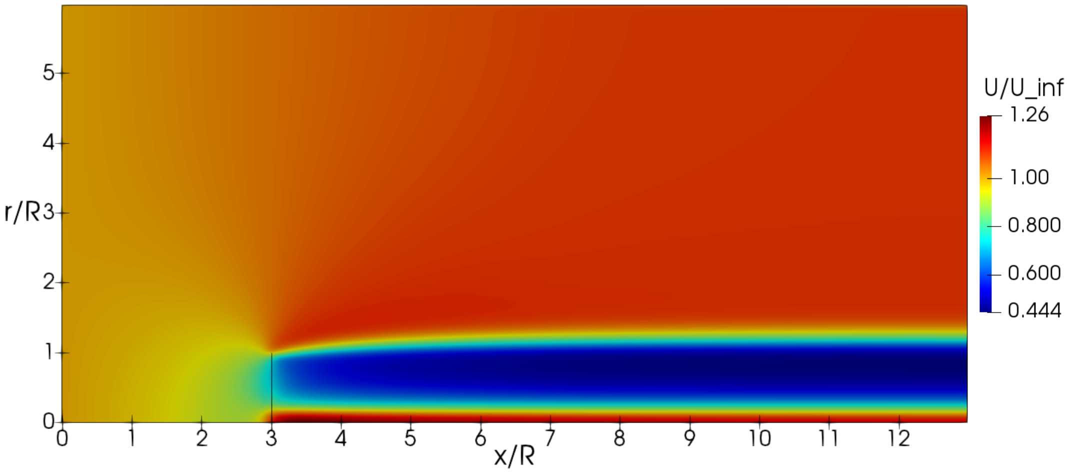

Figure 4.22: Velocity field for $U_\infty = 10\ m/s$. The disc is represented by a straight line.

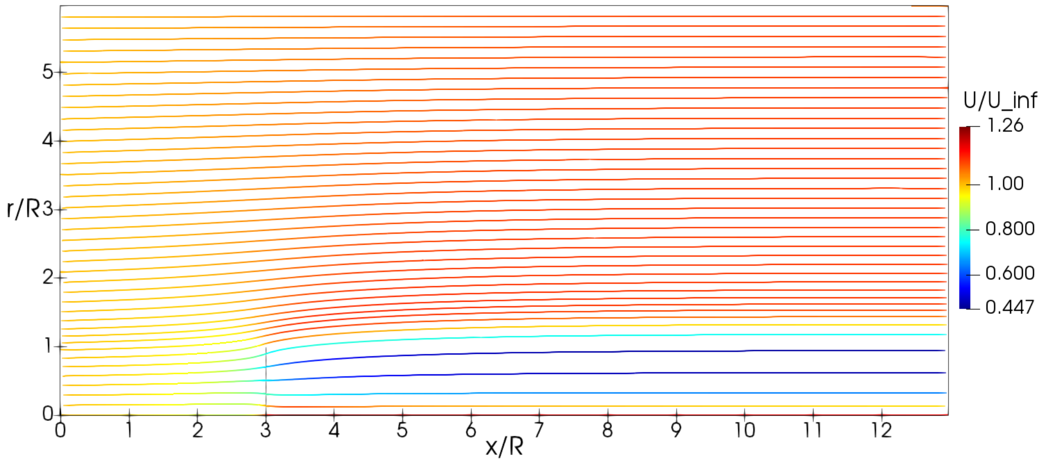

Figure 4.23: Streamlines for $U_\infty = 10\ m/s$. The disc is represented by a straight line.

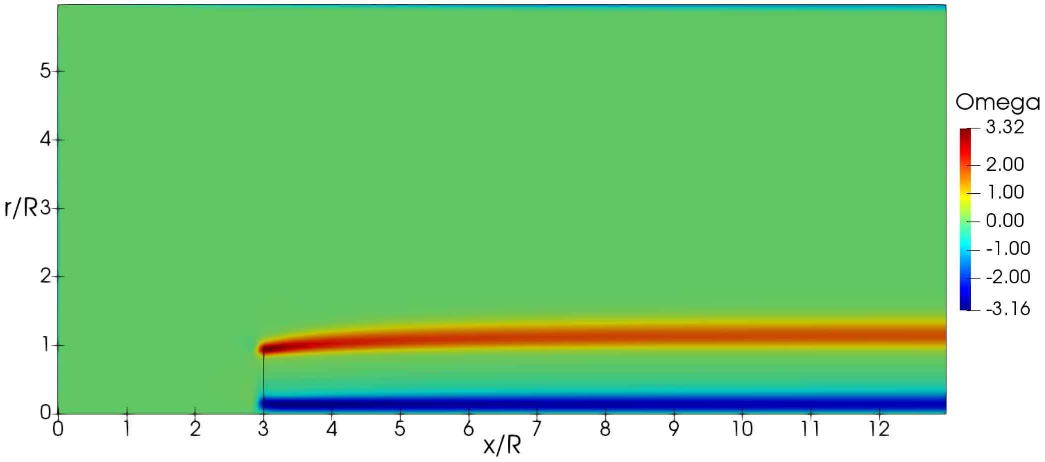

Figure 4.24: Vorticty field for $U_\infty = 10\ m/s$. The disc is represented by a straight line.

when the inflow velocity decreases (see Figure 4.25a). Any remarkable change in the axial velocity is found downstream. In Figure 4.25b, we can see that the rotor presence perturbs the radial velocity five radii downstream, mostly on the tip region. However, it reduces its value by some radii until it achieves approximately zero at $x = 12.9R$. Figure 4.25c shows that the tangential velocity can reach negative values in the inner section for a small inflow. The flow decrease is more remarkable on the maximum of each plot, e.g., for $U_\infty = 15\ m/s$, the maximum near $r/R = 0.2$ is above 0.3, but some radii downstream, it decreases below this value. All the downstream velocities seem to be unable to recover the original values completely. Only the radial velocity regains the upstream velocity; however, this is hardly perturbed by the rotor.

As seen, the presented model can reproduce the characteristics of the flow around the rotor. It is appreciated how the wake expands and the speed increases outside the rotor. Also, about one radius ahead of the rotor, the flow decelerates. On the other hand, a vortex shed is seen at the edge of the rotor, which expands and fades several radii behind. This vortex is caused by the velocity gradient generated near the edge, where the flow over the rotor joins the freestream flow. All these elements are essential to evaluate the performance of turbines interacting with each other and optimize the array of wind turbines.

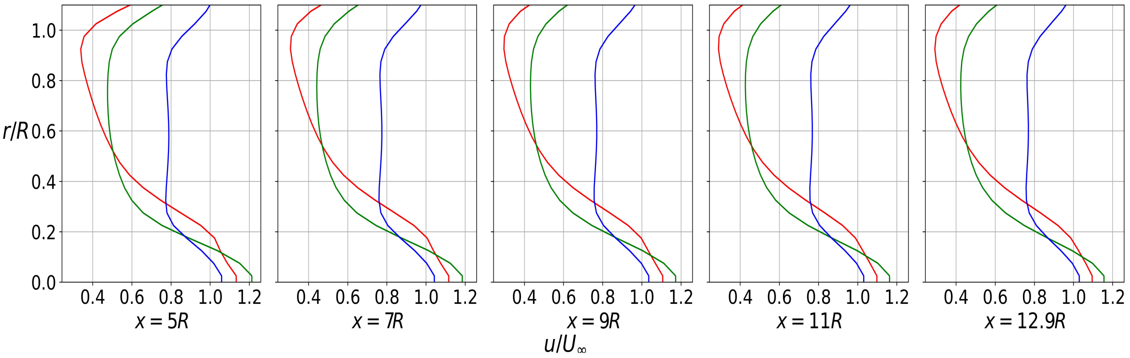

(a) Axial velocity.

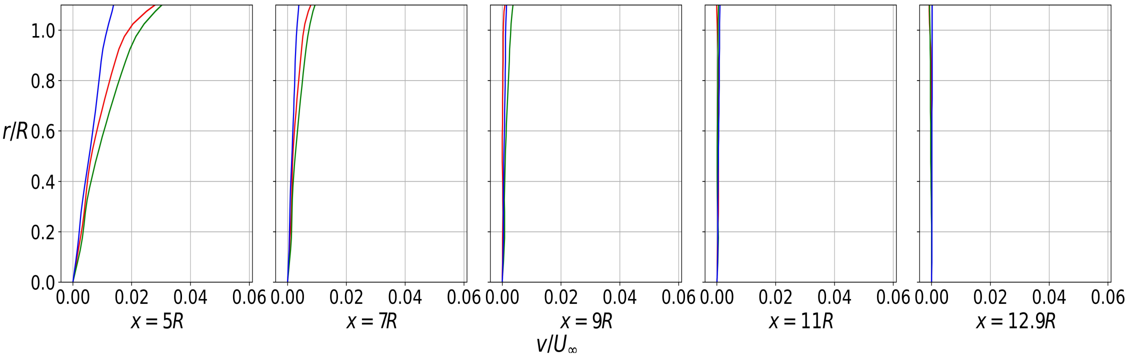

(b) Radial velocity.

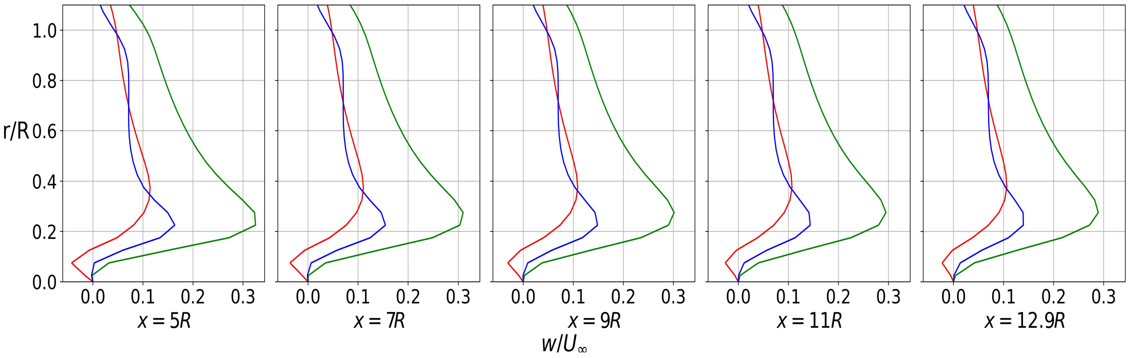

(c) Tangential velocity.

Figure 4.25: Distributions of axial (a), radial (b) and tangential (c) velocities at various downstream locations for three inflow values (red: $U_\infty = 5\ m/s$, green: $U_\infty = 10\ m/s$, blue: $U_\infty = 15\ m/s$).

4.3.2 Hub correction assessment

The hub and nacelle have an impact on the downstream wake behind the rotor, as is investigated by Naderi and Torabi [41]. These two parts represent a solid body that imposes a force on the fluid, which should stop it. However, the hub's influence on the CFD models is usually not taken into account since the power generation on the blades' inner region is minimal. In this model, the actual hub geometry is not considered; however, to get over this obstacle, a hub correction is implemented to consider the behavior of the center of the rotor of the flow field. Nevertheless, the hub correction is applied in both force directions, which could not completely represent the interaction between the rotor and the flow since the maximum axial force should be in the center of the rotor due to the presence of the rigid body of the hub. Besides, the tangential force should decrease because of the small force implemented by the hub rotation.

A similar need for having an independent tip loss factor for each force has been studied by Pirrung et al. [42]. To evaluate the hub loss factor for each force direction, this was implemented for $U_\infty = 10\ m/s$ in three different ways: in both force directions, in the axial force direction only, and without hub correction. Applying the hub loss function just in the axial direction is not necessary to follow the Eqs. 2.48 and 2.49. Instead of implementing the correction on the lift and drag coefficients, it is incorporated directly into the equations for forces as

$$f_x = \frac{1}{4\pi r dx} B\rho V_{rel}^2 c(C_L \text{cos}\phi + C_D \text{sin}\phi)F_{tip} \tag{4.1}$$

$$f_r = 0 \tag{4.2}$$

$$f_\theta = \frac{1}{4\pi r dx} B\rho V_{rel}^2 c(C_L \text{sin}\phi - C_D \text{cos}\phi)F_{hub}F_{tip} \tag{4.3}$$

And the thrust and power are computed following

$$\text{Thrust} = T = \frac{1}{2}\rho B \sum_{k=1}^{k=N} V_{rel_k}^2 c_k (C_{Lk} \text{cos}\phi_k + C_{Dk} \text{sin}\phi_k) dr_k F_{tip} \tag{4.4}$$

$$\text{Power} = P = \frac{1}{2}\rho B\Omega \sum_{k=1}^{k=N} r_k V_{rel_k}^2 c_k (C_{Lk} \text{cos}\phi_k + C_{Dk} \text{sin}\phi_k) dr_k F_{hub} F_{tip} \tag{4.5}$$

The forces acting on the rotor should be different from those presented previously, except for the one corrected in both directions. The comparison between the force distribution is shown in Figure 4.26. The main difference is around the root, up to $r/R = 0.15$. Applying the hub correction makes the axial force lower in the region where the hub should be (see Figure 4.26a). Opposite to this, without hub correction,

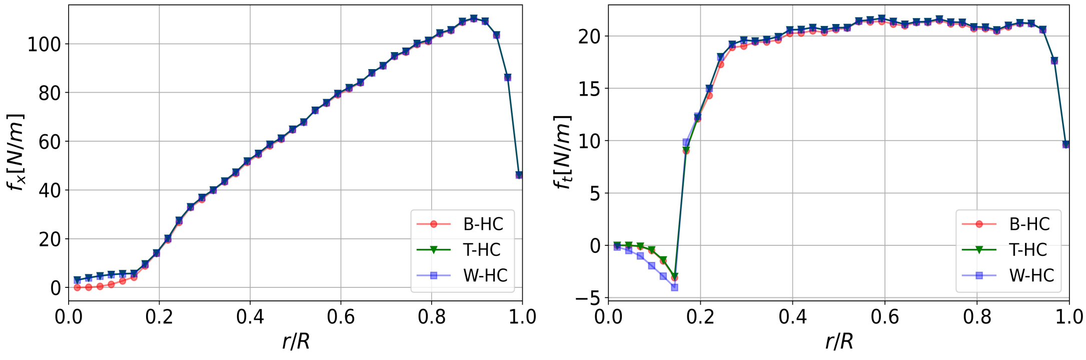

(a) Axial force.

(b) Tangential force.

Figure 4.26: Axial (a) and tangential (b) force in the radial direction. (B-HC: Both force directions corrected; T-HC: Just tangential direction corrected; W-HC: Both force directions without correction).

the axial force is greater, which corresponds more with the presence of the hub. As seen in Figure 4.26b, the tangential force reduces to zero at the center, considering the less force that the hub should impose. The tangential force is lower in the inner spanwise when the hub correction is not applied.

A comparison between the velocities obtained is shown in Figure 4.27. The velocity near $r/R = 0$ applying the correction in both directions is greater than the others (see

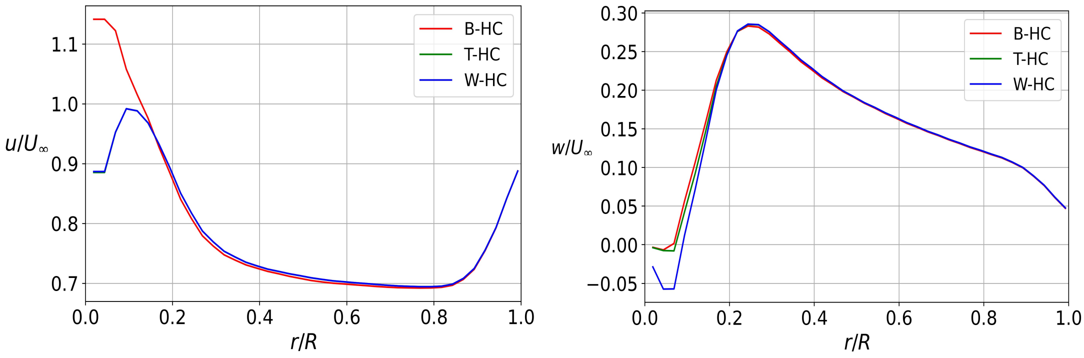

(a) Axial velocity.

(b) Tangential velocity.

Figure 4.27: Axial (a) and tangential (b) velocity in the radial direction. (B-HC: Both force directions corrected; T-HC: Just tangential direction corrected; W-HC: Both force directions without correction).

Figure 4.27a). As was mentioned, the velocity must decrease in this region because of the rotor presence. Around $r/R = 0.1$, the axial velocity tends to increase, almost reaching the upstream velocity. Out of the hub region, the behavior for all the cases is similar. On the other hand, in Figure 4.27b, the tangential velocity is affected when no correction is applied; therefore, it achieves lower values in this region, which means that the force is less there. The hub correction reduces the tangential force on the hub, so the tangential velocity is not incremented. Besides, not applying the hub correction in the axial direction increases the force in this direction, so the axial velocity decreases.

The axial velocity flow field imposing the several configurations of the tip correction can be appreciated in Figure 4.28. The flow fields are similar when the hub loss factor is set for just the tangential direction and with no correction. Figure 4.28a shows that the velocity in the center of the rotor is incremented when the hub correction is applied in the axial direction; this corresponds to the fact that no solid body stands in the way of the flow. Moreover, the flow is disrupted when the hub correction is missing, reducing the velocity of the center. There is a need to incorporate a new hub correction that analytically can reproduce the actual presence of the hub. Otherwise, considering the real geometry of the hub and nacelle, although it requires a more complex model. According to Yang and Sotiropoulos [18] and Naderi and Torabi [41], when the hub and nacelle are incorporated into the model, it is noted the reduction of the velocity on the center of the rotor. This reduction is alike to the behavior found by not implementing the hub correction in the axial direction, as seen in Figures 4.28b and 4.28c. Both the hub and the nacelle represent an obstacle to the fluid and affect the flow field behind the rotor.

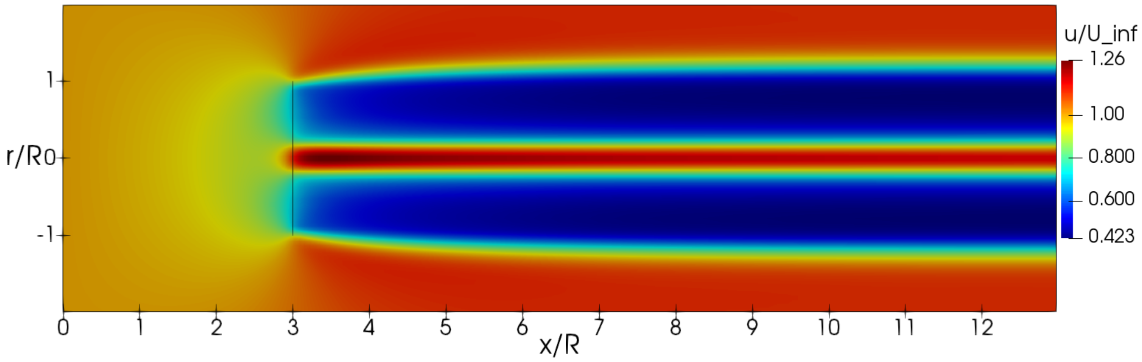

(a) Hub correction in both directions.

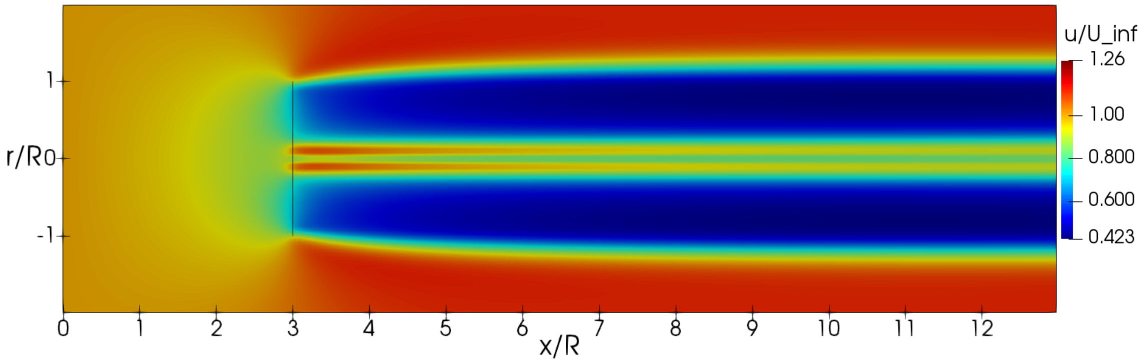

(b) Hub correction just in tangential direction.

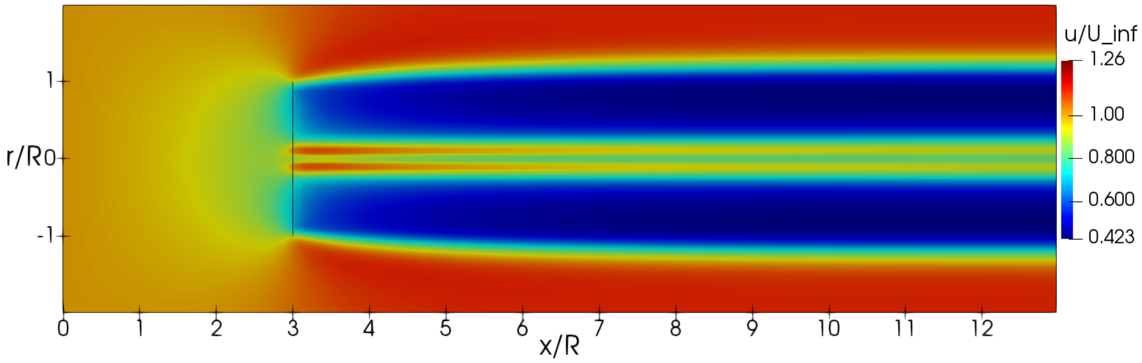

(c) Without hub correction.

Figure 4.28: Axial velocity applying hub correction in both directions (a), just tangential direction (b) and without correction (c). The flow field is mirrored to appreciate the hub interaction. The disc is represented by a straight line.

Chapter 5

Conclusions

This thesis presents the numerical simulation of the rotor's aerodynamics of a horizontal axis wind turbine. The study is based on the actuator disc concept, the blade element theory, the immersed boundary method, and the Navier-Stokes equations for an incompressible and approximately inviscid fluid with axial symmetry.

First, a study of the numerical domain is researched to reduce the time of the simulations. The results showed that the radial length is more important than the axial length. The axial factor taken as the test parameter oscillates inside a small range of values from a certain radial length, namely, $L_R = 6R$. Besides, varying the axial length beyond ten radii behind the rotor has no major effect on the results. The computational time is studied to know when the steady-state is obtained. The results showed that the flow gets stable at $t^* = 20$. After this value, the results are roughly similar. Thus, the computational time can be constrained to save computational time.

In order to assess the CFD model, this was compared against the one-dimensional momentum theory results, taking the same initial conditions. The results showed that the axial factor is constant in almost all tests, but near the tip, it increases, and the velocity tends to recover the upstream velocity. The velocity gradient occurring on the tip induces a vortex shed, which expands and dissipates behind the rotor. The vortex shed should be deeper studied to understand the interaction with other rotors in a wind farm. Moreover, we found that the velocity decreases behind the rotor while the wake expands. The one-dimensional momentum theory neglects the radial velocity variation on the rotor plane. However, the study shows that the radial velocity changes on the rotor plane. Inside the Navier-Stokes equations, the radial change can modify the velocity in other directions. Thus, the general flow field on each blade element is disturbed. As a result, the blade element properties change, and the wind turbine's general performance is affected. Therefore, we can conclude that the one-dimensional theory does not completely consider the actual flow behavior occurring on the rotor.

A CFD model is proposed to simulate the wind turbine rotor aerodynamic performance under several incoming velocities. The actual geometry of the baseline NREL wind turbine was used. The axial velocity remains constant on most of the rotor for velocities above 10 m/s. Near the tip, the axial velocity tends to recover the upstream inflow speed. For all the different upstream velocities, the tangential velocity shows an increment until where the lifting surface is, then it starts to decrease to zero. The maximum tangential velocity occurs roughly on the transition from the cylinder to the airfoil. The computed axial forces show an increment throughout the rotor, but these declines close to the tip. Besides, the tangential forces remain constant throughout the rotor for lower incoming velocities. On the other hand, the tangential force tends to be unstable throughout the rotor when the upstream speed grows. Thus, the proposed model provides information about the loads on the rotor and can be used to optimize the blade geometry. The power production and the thrust predicted are compared against BEM results and experimental data. The power predicted by the CFD model agrees better than the BEM results. CFD model achieves up to a relative error of 43.73% in the cut-in speed region, while the BEM method results in a relative error of 674.80%. In the transition zone, for $U_\infty = 7.5$ m/s, the relative errors are 16.37% and 21.18% for the CFD model and the BEM method, respectively. In the rated output region, the power is similar in both results. The minimum error within the entire thrust curve obtained for the CFD model is 74.54%, while for the BEM method is 266.74%. Therefore, the computational model presented becomes a tool more reliable than the BEM method commonly used to predict the performance of a wind turbine rotor. Nevertheless, both power and thrust resulting from the CFD model deviate for larger inflow velocities than 12 m/s. In this last region of larger inflow speeds, the turbulent effects can be more important in the flow behavior and, therefore, rotor performance. Because of that, it becomes necessary to explore a turbulence model to incorporate the actual physics of the flow.

An assessment of the hub correction is presented. Incorporating the hub correction into the force equations increases the axial velocity in the zone near the rotor center. However, the axial velocity decreases when the hub correction is missing, which agrees with the lower velocity expected due to the presence of a solid body such as the hub. Although the power generated in the center of the rotor is minimal, the flow field prediction can be affected by the correct modeling of the hub. Therefore, deeper incorporation of the hub should be studied.

There are still unsolved problems with the dynamic of a wind turbine rotor. The numerical tool developed in this work aims to predict the rotor performance and understand the main phenomena occurring in the flow field. This work is the first step to modeling the interaction of wind turbines in wind farms. The complexity of the problem, such as the turbulence, demands new approaches to understanding the physics behind the flow to adapt solutions to actual applications.

Appendix A

Supplementary data

A.1 Airfoil data

Table A.1: S809 airfoil data.

α	C_L	C_D	α	C_L	C_D	α	C_L	C_D
-180	-0.0361	0.0060	-158	0.5495	0.2363	-136	0.7014	0.7958
-179	0.0577	0.0065	-157	0.5657	0.2566	-135	0.6974	0.8243
-178	0.1474	0.0080	-156	0.5812	0.2775	-134	0.6925	0.8528
-177	0.2257	0.0105	-155	0.5959	0.2990	-133	0.6867	0.8812
-176	0.2837	0.0140	-154	0.6099	0.3212	-132	0.6800	0.9095
-175	0.3176	0.0185	-153	0.6229	0.3441	-131	0.6725	0.9378
-174	0.3322	0.0240	-152	0.6352	0.3675	-130	0.6641	0.9659
-173	0.3367	0.0304	-151	0.6465	0.3914	-129	0.6548	0.9938
-172	0.3388	0.0379	-150	0.6569	0.4159	-128	0.6448	1.0215
-171	0.3429	0.0462	-149	0.6663	0.4409	-127	0.6340	1.0490
-170	0.3502	0.0556	-148	0.6748	0.4663	-126	0.6224	1.0762
-169	0.3607	0.0659	-147	0.6824	0.4922	-125	0.6100	1.1031
-168	0.3740	0.0771	-146	0.6890	0.5184	-124	0.5969	1.1296
-167	0.3893	0.0892	-145	0.6946	0.5451	-123	0.5831	1.1558
-166	0.4061	0.1022	-144	0.6992	0.5720	-122	0.5687	1.1816
-165	0.4238	0.1161	-143	0.7029	0.5993	-121	0.5535	1.2069
-164	0.4421	0.1308	-142	0.7055	0.6268	-120	0.5378	1.2317
-163	0.4606	0.1464	-141	0.7072	0.6546	-119	0.5214	1.2561
-162	0.4790	0.1628	-140	0.7080	0.6826	-118	0.5044	1.2799
-161	0.4973	0.1801	-139	0.7078	0.7107	-117	0.4869	1.3032
-160	0.5152	0.1981	-138	0.7066	0.7390	-116	0.4688	1.3259
-159	0.5326	0.2168	-137	0.7044	0.7674	-115	0.4502	1.3479

Continued on next page

α	C_L	C_D	α	C_L	C_D	α	C_L	C_D
-114	0.4312	1.3694	-73	-0.4508	1.4994	-32	-0.6174	0.4654
-113	0.4117	1.3901	-72	-0.4677	1.4831	-31	-0.6069	0.4399
-112	0.3917	1.4102	-71	-0.4841	1.4660	-30	-0.5959	0.4148
-111	0.3706	1.4296	-70	-0.5000	1.4481	-29	-0.5843	0.3902
-110	0.3499	1.4482	-69	-0.5153	1.4295	-28	-0.5723	0.3661
-109	0.3288	1.4661	-68	-0.5301	1.4101	-27	-0.5598	0.3425
-108	0.3074	1.4831	-67	-0.5443	1.3901	-26	-0.5471	0.3195
-107	0.2857	1.4994	-66	-0.5579	1.3693	-25	-0.5341	0.2971
-106	0.2638	1.5149	-65	-0.5710	1.3478	-24	-0.5211	0.2752
-105	0.2415	1.5295	-64	-0.5834	1.3258	-23	-0.5082	0.2540
-104	0.2191	1.5432	-63	-0.5952	1.3031	-22	-0.4958	0.2333
-103	0.1965	1.5561	-62	-0.6064	1.2798	-21	-0.4842	0.2132
-102	0.1737	1.5681	-61	-0.6170	1.2560	-20	-0.4741	0.1938
-101	0.1507	1.5792	-60	-0.6269	1.2316	-19	-0.4663	0.1749
-100	0.1277	1.5894	-59	-0.6362	1.2068	-18	-0.4622	0.1565
-99	0.1045	1.5986	-58	-0.6448	1.1814	-17	-0.4637	0.1385
-98	0.0813	1.6069	-57	-0.6527	1.1557	-16	-0.4739	0.1208
-97	0.0581	1.6142	-56	-0.6599	1.1295	-15	-0.4974	0.1032
-96	0.0348	1.6206	-55	-0.6664	1.1029	-14	-0.5407	0.0855
-95	0.0116	1.6260	-54	-0.6722	1.0760	-13	-0.6104	0.0676
-94	-0.0117	1.6305	-53	-0.6774	1.0488	-12	-0.7073	0.0500
-93	-0.0348	1.6339	-52	-0.6818	1.0213	-11	-0.8124	0.0341
-92	-0.0579	1.6364	-51	-0.6854	0.9936	-10	-0.8796	0.0227
-91	-0.0808	1.6379	-50	-0.6884	0.9657	-9	-0.8691	0.0167
-90	-0.1037	1.6384	-49	-0.6906	0.9376	-8	-0.7897	0.0147
-89	-0.1264	1.6379	-48	-0.6921	0.9093	-7	-0.6785	0.0141
-88	-0.1489	1.6364	-47	-0.6929	0.8809	-6	-0.5607	0.0138
-87	-0.1712	1.6339	-46	-0.6929	0.8525	-5	-0.4437	0.0085
-86	-0.1932	1.6304	-45	-0.6922	0.8240	-4.5	-0.3806	0.0096
-85	-0.2151	1.6260	-44	-0.6908	0.7955	-4	-0.3230	0.0098
-84	-0.2367	1.6206	-43	-0.6886	0.7670	-3.5	-0.2646	0.0102
-83	-0.2579	1.6142	-42	-0.6857	0.7386	-3	-0.2056	0.0103
-82	-0.2789	1.6069	-41	-0.6820	0.7103	-2.5	-0.1466	0.0103
-81	-0.2996	1.5986	-40	-0.6776	0.6821	-2	-0.0878	0.0104
-80	-0.3199	1.5893	-39	-0.6725	0.6541	-1	0.0302	0.0104
-79	-0.3398	1.5792	-38	-0.6667	0.6263	-0.5	0.0888	0.0105
-78	-0.3594	1.5681	-37	-0.6602	0.5987	0	0.1473	0.0106
-77	-0.3786	1.5561	-36	-0.6530	0.5714	0.5	0.2058	0.0107
-76	-0.3973	1.5432	-35	-0.6450	0.5444	1	0.2650	0.0107
-75	-0.4156	1.5294	-34	-0.6365	0.5177	1.5	0.3234	0.0109
-74	-0.4335	1.5148	-33	-0.6272	0.4914	2	0.3817	0.0111

Continued on next page

α	C_L	C_D	α	C_L	C_D	α	C_L	C_D
2.5	0.4416	0.0109	32	0.8830	0.4594	73	0.6733	1.5235
3	0.5023	0.0106	33	0.8917	0.4864	74	0.6486	1.5394
3.5	0.5634	0.0102	34	0.9005	0.5138	75	0.6231	1.5544
4	0.6242	0.0097	35	0.9093	0.5415	76	0.5968	1.5686
4.5	0.6847	0.0093	36	0.9180	0.5695	77	0.5698	1.5818
5	0.7433	0.0091	37	0.9263	0.5978	78	0.5420	1.5942
5.5	0.8010	0.0089	38	0.9343	0.6263	79	0.5135	1.6056
6	0.8469	0.0093	39	0.9418	0.6550	80	0.4844	1.6161
6.5	0.8728	0.0113	40	0.9487	0.6839	81	0.4546	1.6256
7	0.9015	0.0128	41	0.9551	0.7129	82	0.4242	1.6341
7.5	0.9292	0.0139	42	0.9608	0.7420	83	0.3932	1.6417
8	0.9525	0.0148	43	0.9657	0.7713	84	0.3618	1.6483
8.5	0.9753	0.0160	44	0.9699	0.8005	85	0.3298	1.6539
9	0.9944	0.0175	45	0.9732	0.8298	86	0.2974	1.6584
9.5	1.0100	0.0196	46	0.9758	0.8591	87	0.2646	1.6620
10.5	1.0580	0.0237	47	0.9774	0.8883	88	0.2314	1.6646
11	1.0782	0.0263	48	0.9782	0.9174	89	0.1979	1.6661
11.5	1.0864	0.0299	49	0.9780	0.9465	90	0.1641	1.6667
12	1.0981	0.0333	50	0.9769	0.9753	91	0.1300	1.6662
12.5	1.1032	0.0374	51	0.9748	1.0040	92	0.0958	1.6647
13	1.1106	0.0412	52	0.9717	1.0325	93	0.0614	1.6622
13.5	1.1108	0.0461	53	0.9676	1.0607	94	0.0269	1.6586
14	1.1174	0.0506	54	0.9625	1.0886	95	-0.0076	1.6541
14.5	1.1255	0.0551	55	0.9564	1.1162	96	-0.0422	1.6486
15	1.1295	0.0602	56	0.9492	1.1435	97	-0.0768	1.6420
16	1.0746	0.0868	57	0.9411	1.1704	98	-0.1112	1.6345
17	1.0224	0.1053	58	0.9319	1.1968	99	-0.1455	1.6260
18	0.9764	0.1250	59	0.9216	1.2228	100	-0.1797	1.6165
19	0.9380	0.1456	60	0.9104	1.2484	101	-0.2137	1.6061
20	0.9074	0.1668	61	0.8981	1.2734	102	-0.2473	1.5948
21	0.8841	0.1887	62	0.8847	1.2978	103	-0.2807	1.5825
22	0.8673	0.2111	63	0.8704	1.3218	104	-0.3137	1.5693
23	0.8560	0.2339	64	0.8550	1.3451	105	-0.3463	1.5552
24	0.8493	0.2572	65	0.8386	1.3677	106	-0.3784	1.5402
25	0.8464	0.2810	66	0.8213	1.3898	107	-0.4101	1.5244
26	0.8465	0.3052	67	0.8029	1.4111	108	-0.4412	1.5077
27	0.8491	0.3299	68	0.7836	1.4317	109	-0.4717	1.4902
28	0.8537	0.3549	69	0.7634	1.4516	110	-0.5016	1.4719
29	0.8596	0.3805	70	0.7422	1.4708	108	-0.4412	1.5077
30	0.8667	0.4064	71	0.7201	1.4892	109	-0.4717	1.4902
31	0.8746	0.4327	72	0.6971	1.5067	110	-0.5016	1.4719

Continued on next page

α	C_L	C_D	α	C_L	C_D	α	C_L	C_D
111	-0.5309	1.4528	135	-0.9432	0.8344	159	-0.6713	0.2181
112	-0.5594	1.4330	136	-0.9455	0.8054	160	-0.6481	0.1992
113	-0.5871	1.4124	137	-0.9465	0.7765	161	-0.6245	0.1810
114	-0.6141	1.3912	138	-0.9462	0.7476	162	-0.6005	0.1637
115	-0.6430	1.3692	139	-0.9446	0.7188	163	-0.5762	0.1471
116	-0.6682	1.3466	140	-0.9417	0.6902	164	-0.5518	0.1314
117	-0.6926	1.3234	141	-0.9376	0.6618	165	-0.5273	0.1166
118	-0.7160	1.2996	142	-0.9322	0.6335	166	-0.5030	0.1026
119	-0.7384	1.2752	143	-0.9256	0.6055	167	-0.4790	0.0895
120	-0.7598	1.2503	144	-0.9177	0.5778	168	-0.4555	0.0773
121	-0.7802	1.2249	145	-0.9086	0.5505	169	-0.4328	0.0661
122	-0.7995	1.1990	146	-0.8984	0.5234	170	-0.4110	0.0557
123	-0.8177	1.1727	147	-0.8870	0.4968	171	-0.3903	0.0464
124	-0.8348	1.1459	148	-0.8744	0.4706	172	-0.3708	0.0379
125	-0.8508	1.1188	149	-0.8607	0.4448	173	-0.3520	0.0305
126	-0.8656	1.0914	150	-0.8460	0.4195	174	-0.3330	0.0240
127	-0.8792	1.0636	151	-0.8302	0.3947	175	-0.3116	0.0185
128	-0.8916	1.0356	152	-0.8134	0.3704	176	-0.2842	0.0140
129	-0.9027	1.0073	153	-0.7956	0.3467	177	-0.2457	0.0105
130	-0.9126	0.9788	154	-0.7769	0.3237	178	-0.1917	0.0080
131	-0.9213	0.9501	155	-0.7573	0.3012	179	-0.1208	0.0065
132	-0.9287	0.9213	156	-0.7369	0.2794	180	-0.0361	0.0060
133	-0.9348	0.8924	157	-0.7157	0.2583			
134	-0.9396	0.8634	158	-0.6938	0.2378			

A.2 Blade geometry

Table A.2: Blade geometry of NREL Baseline.

Radius (m)	**Chord** (m)	**Twist** ($^\circ$)	**Radius** (m)	**Chord** (m)	**Twist** ($^\circ$)
0.096	0.218	0.000	2.606	0.600	3.574
0.221	0.218	0.000	2.732	0.588	3.048
0.347	0.218	0.000	2.857	0.575	2.569
0.472	0.218	0.000	2.983	0.562	2.131
0.598	0.218	0.000	3.109	0.549	1.729
0.723	0.218	0.000	3.234	0.537	1.359
0.849	0.340	29.822	3.360	0.524	1.015
0.974	0.461	27.457	3.485	0.511	0.691
1.100	0.583	24.538	3.611	0.499	0.383
1.225	0.705	21.049	3.736	0.486	0.084
1.351	0.730	17.395	3.862	0.474	-0.208
1.477	0.715	14.899	3.987	0.461	-0.493
1.602	0.702	12.615	4.113	0.449	-0.765
1.728	0.689	10.637	4.238	0.436	-1.020
1.853	0.676	8.982	4.364	0.423	-1.249
1.979	0.664	7.622	4.489	0.411	-1.446
2.104	0.651	6.510	4.615	0.398	-1.610
2.230	0.638	5.593	4.741	0.385	-1.746
2.355	0.626	4.822	4.866	0.372	-1.863
2.481	0.613	4.159	4.992	0.360	-1.970

Bibliography

[1] Hero, *The Pneumatics of Hero of Alexandria, from the original Greek.* London: Taylor, Walton and Maberly, 1851. 1

[2] "Los molinos de viento persas de 1000 años, que pueden dejar de funcionar por falta de relevo." https://ecoinventos.com/molinos-de-viento-persas-de-nashtifan/, 2018. xi, 2

[3] T. J. Price, "James blyth — britain's first modern wind power pioneer," *Wind Engineering*, vol. 29, no. 3, pp. 191–200, 2005. xi, 2

[4] P. Veers, K. Dykes, E. Lantz, S. Barth, C. L. Bottasso, O. Carlson, A. Clifton, J. Green, P. Green, H. Holttinen, D. Laird, V. Lehtomäki, J. K. Lundquist, J. Manwell, M. Marquis, C. Meneveau, P. Moriarty, X. Munduate, M. Muskulus, J. Naughton, L. Pao, J. Paquette, J. Peinke, A. Robertson, J. S. Rodrigo, A. M. Sempreviva, J. C. Smith, A. Tuohy, and R. Wiser, "Grand challenges in the science of wind energy," *Science*, vol. 366, no. 6464, p. eaau2027, 2019. 3, 4

[5] S. Naderi, S. Parvanehmasiha, and F. Torabi, "Modeling of horizontal axis wind turbine wakes in horns rev offshore wind farm using an improved actuator disc model coupled with computational fluid dynamic," *Energy Conversion and Management*, vol. 171, pp. 953–968, 2018. 3

[6] J. O. Dabiri, J. R. Greer, J. R. Koseff, P. Moin, and J. Peng, "A new approach to wind energy: Opportunities and challenges," *AIP Conference Proceedings*, vol. 1652, no. 1, pp. 51–57, 2015. 4

[7] A. Betz, "Das maximum der theoretisch möglichen ausnützung des windes durch windmotoren," *Zeitschrift für das gesamte Turbinenwesen*, vol. 26, pp. 307–309, 1920. 4, 7

[8] H. Glauert, "Airplane propellers," *In: Durand, W.F. (ed.) Aerodynamic theory (Division L)*, vol. vol. IV, pp. 169–360, 1935. 4, 7

[9] N. E. Joukowsky, "Vortex theory of a rowing screw," *Trudy Otdeleniya Fizicheskikh Nauk Obshchestva Lubitelei Estestvoznaniya*, vol. 16, p. 1, 1912. 4

[10] T. Burton, D. Sharpe, N. Jenkins, and E. Bossanyi, *Wind Energy Handbook*. New York: Wiley, 2002. 4

[11] J. N. Sørensen and C. W. Kock, "A model for unsteady rotor aerodynamics," *Journal of Wind Engineering and Industrial Aerodynamics*, vol. 58, no. 3, pp. 259–275, 1995. 4

[12] R. Mikkelsen, *Actuator Disc Methods Applied to Wind Turbines*. PhD thesis, Jan. 2004. 4

[13] A. Behrouzifar and M. Darbandi, "An improved actuator disc model for the numerical prediction of the far-wake region of a horizontal axis wind turbine and its performance," *Energy Conversion and Management*, vol. 185, pp. 482–495, 04 2019. xi, 4, 10

[14] J. N. Sorensen and W. Z. Shen, "Numerical Modeling of Wind Turbine Wakes ," *Journal of Fluids Engineering*, vol. 124, pp. 393–399, 05 2002. 4

[15] A. Rodeyna, D. Ivan, and M. Fawaz, "Determination of wind turbine far wake using actuator disk," *Valencia Global 2014, Escuela Técnica Superior de Ingeniería del Diseño*, pp. 254–260, 06 2014. 4

[16] W. Z. Shen, J. N. Sørensen, and R. Mikkelsen, "Tip Loss Correction for Actuator/Navier–Stokes Computations ," *Journal of Solar Energy Engineering*, vol. 127, pp. 209–213, 04 2005. 4

[17] L. Martínez Tossas, S. Leonardi, M. Churchfield, and P. Moriarty, "A comparison of actuator disk and actuator line wind turbine models and best practices for their use," 01 2012. 4

[18] X. Yang and F. Sotiropoulos, "A new class of actuator surface models for wind turbines," *Wind Energy*, vol. 21, no. 5, pp. 285–302, 2018. 5, 53

[19] J. Sørensen, *General Momentum Theory for Horizontal Axis Wind Turbines*. PhD thesis, 2016. xi, 7, 8, 12

[20] R. E. Froude, "On the part played in propulsion by difference in pressure," *Transactions of the Institution of Naval Architects*, vol. 30, pp. 390–423, 1889. 7

[21] W. J. M. Rankine, "On the mechanical principles of the action of propellers," *Transactions of the Institution of Naval Architects*, vol. 6, pp. 13–39, 1865. 7

[22] S. Perez-Becker, F. Papi, J. Saverin, D. Marten, A. Bianchini, and C. O. Paschereit, "Is the blade element momentum theory overestimating wind turbine loads? – an aeroelastic comparison between openfast's aerodyn and qblade's lifting-line free vortex wake method," *Wind Energy Science*, vol. 5, no. 2, pp. 721–743, 2020. 7

[23] J. Manwell and et. al, *Wind Energy Explained: theory, design, and application*. WILEY, 2 th ed., 2009. 7, 12, 16

[24] D. Wood, *Blade Element Theory for Wind Turbines*, pp. 41–55. London: Springer London, 2011. 12

[25] M. Clifton-Smith, “Wind turbine blade optimisation with tip loss corrections,” *Wind Engineering*, vol. 33, pp. 477–496, 10 2009. 15

[26] W. Z. Shen, J. Sørensen, and R. Mikkelsen, “Tip loss correction for actuator/-navier–stokes computations,” *Journal of Solar Energy Engineering-transactions of The Asme - J SOL ENERGY ENG*, vol. 127, 05 2005. 15

[27] W. Z. Shen, R. Mikkelsen, J. N. Sørensen, and C. Bak, “Tip loss corrections for wind turbine computations,” *Wind Energy*, vol. 8, no. 4, pp. 457–475, 2005. 15

[28] W. Z. Shen, J. N. Sørensen, and R. Mikkelsen, “Tip Loss Correction for Actuator/Navier–Stokes Computations ,” *Journal of Solar Energy Engineering*, vol. 127, pp. 209–213, 04 2005. 15

[29] J. Sørensen, K. Nilsson, S. Ivanell, H. Asmuth, and R. Mikkelsen, “Analytical body forces in numerical actuator disc model of wind turbines,” *Renewable Energy*, vol. 147, pp. 2259–2271, 2019. 15, 16

[30] M. L. Buhl, Jr, “New empirical relationship between thrust coefficient and induction factor for the turbulent windmill state,” 8 2005. xi, 16, 17

[31] V. H. K. and M. W., *An Introduction to Computational Fluid Dynamics: The Finite Volume Method.* Pearson Education Limited, 2007. 20

[32] H. Luo, *Immersed Boundary Method*, pp. 805–808. Boston, MA: Springer US, 2008. 24

[33] S. Piedra González and E. Ramos Mora, *Simulación numérica de la dinámica de burbujas en dos dimensiones.* 2011. xi, 25

[34] C. S. Peskin, “Flow patterns around heart valves: A numerical method,” *Journal of Computational Physics*, vol. 10, no. 2, pp. 252–271, 1972. 25

[35] D. M. Somers, “Design and experimental results for the s809 airfoil,” 1 1997. 29

[36] W. Timmer and C. Bak, “4 - aerodynamic characteristics of wind turbine blade airfoils,” in *Advances in Wind Turbine Blade Design and Materials* (P. Brøndsted and R. P. Nijssen, eds.), Woodhead Publishing Series in Energy, pp. 109–149, Woodhead Publishing, 2013. 29

[37] M. Hand, D. Simms, L. Fingersh, D. Jager, J. Cotrell, S. Schreck, and S. Larwood, “Unsteady aerodynamics experiment phase vi: Wind tunnel test configurations and available data campaigns,” 01 2001. 30

[38] B. Montgomerie, “Methods for root effects, tip effects and extending the angle of attack range to+-180°,” *Swedish Defence Research Agency*, 2004. 31

[39] J. N. Sørensen, W. Z. Shen, and X. Munduate, “Analysis of wake states by a full-field actuator disc model,” *Wind Energy*, vol. 1, no. 2, pp. 73–88, 1998. 34

[40] P. Giguere and M. S. Selig, “Design of a tapered and twisted blade for the nrel combined experiment rotor,” 4 1999. 38

[41] S. Naderi and F. Torabi, “Numerical investigation of wake behind a hawt using modified actuator disc method,” *Energy Conversion and Management*, vol. 148, pp. 1346–1357, 2017. 51, 53

[42] G. R. Pirrung, M. P. van der Laan, N. Ramos-García, and A. R. Meyer Forsting, “A simple improvement of a tip loss model for actuator disc simulations,” *Wind Energy*, vol. 23, no. 4, pp. 1154–1163, 2020. 51